

We are IntechOpen, the world's leading publisher of Open Access books Built by scientists, for scientists

6,900

Open access books available

186,000

International authors and editors

200M

Downloads

Our authors are among the

154

Countries delivered to

TOP 1%

most cited scientists

12.2%

Contributors from top 500 universities



WEB OF SCIENCE™

Selection of our books indexed in the Book Citation Index
in Web of Science™ Core Collection (BKCI)

Interested in publishing with us?
Contact book.department@intechopen.com

Numbers displayed above are based on latest data collected.
For more information visit www.intechopen.com



LWIR Photodiodes and Focal Plane Arrays Based on Novel HgCdTe/CdZnTe/GaAs Heterostructures Grown by MBE Technique

V. V. Vasiliev, V. S. Varavin, S. A. Dvoretzky,
I. M. Marchishin, N. N. Mikhailov, A. V. Predein,
I. V. Sabinina, Yu. G. Sidorov, A. O. Suslyakov and
A. L. Aseev

Additional information is available at the end of the chapter

<http://dx.doi.org/10.5772/50822>

1. Introduction

Thermal imagers based on the photo detectors for infrared (IR) wavelength range of 3–12 μm are required for applications both in the military equipment for systems of night vision, detection and guidance as well as in the national economy for the medical, agricultural, chemical, metallurgical, fuel industries and others. Nowadays, the leading place among materials for the production of IR photo detectors is occupied by mercury–cadmium–telluride (MCT) solid solutions. This fact is due to the physical properties of these solutions (high speed, the possibility of varying an MCT band gap within a wide range, and high quantum efficiency in the range of overlapping wavelengths). For the last 25 years, the technology of MCT production has been developed intensively, which has made it possible to pass from manufacturing bulk single crystals of relatively small diameters (less than 10 mm) to epilayers on large in diameter substrates (up to 150 mm). The MCT epilayers on large-diameter substrates are necessary for the production of IR PD arrays with a large number of elements for enhancing the production efficiency and reducing the cost of devices. According to this, stringent requirements are imposed on the epitaxial technologies of producing such an MCT material. They include a high structural quality and uniformity of photoelectric characteristics over the entire area. MCT layers on alternative substrates primarily due to its low growth temperatures (~ 180 °C), which prevents the diffusion of impurities from the substrate and reduces the background doping with these impurities. The great successes had

been reached in development of growth MCT HES by MBE on GaAs and Si large in diameter substrate. The decision of fundamental physical and chemical investigations and technological developments allows to fabricate high quality MCT HES on GaAs substrate. Such MCT HES are widely used for developments and production of different formats linear and matrix IR detectors sensitive in separate spectral IR ranges.

In this chapter the results of studies of technological processes at growth MCT HES on (013)GaAs by MBE, the developments of HES design and fabrication on its basis of high quality IR detectors of different applications for IR radiation registration in spectral long wavelength range (LWIR) 8-11 μm .

2. The technological processes of MCT HES growth on (013)GaAs substrates

Fig. 1 showed the scheme of MCT HES included ZnTe and CdTe buffer and adsorber layers in sequence grown on (013)GaAs substrate by MBE.

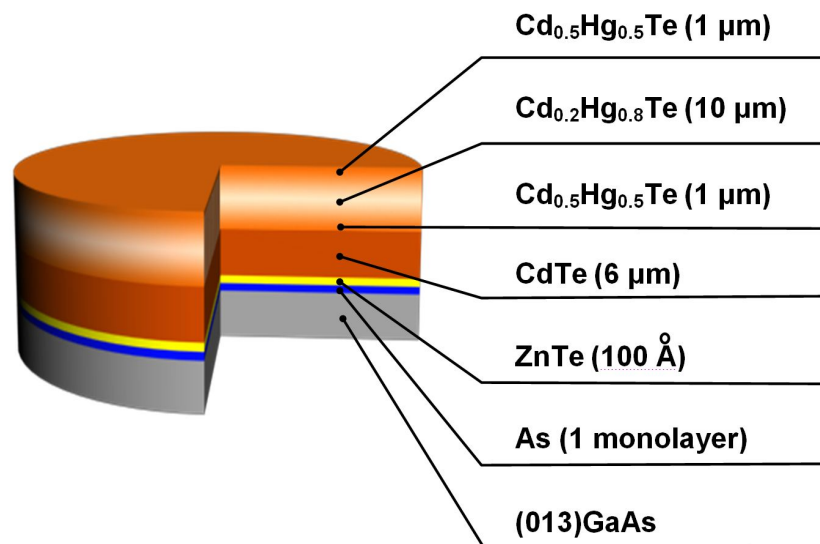


Figure 1. The scheme of MCT HES on (013) GaAs substrate.

The technology of growth MCT HES includes the following processes:

- the preepitaxial preparation of surface substrate;
- the growth of ZnTe and CdTe buffer layers;
- the growth of MCT absorber layer with special design.

2.1. The preepitaxial preparation of surface substrate

The GaAs substrate surface before epitaxial growth must be atomically smooth and clean.

For this purpose the preepitaxial substrate surface preparation included the chemical etching process and thermal cleaning process in ultra-high vacuum at 500÷600 °C.

We used (013)GaAs substrates 2" and 3" in diameter which initially prepared as epi-ready. Nevertheless it is necessary to remove the defects surface layer which prevents the epitaxial growth of high quality MCT HES. The study of chemical etching of GaAs in sulfuric acid etchant [1] allows to determine optimal conditions for preparation GaAs surface. Fig. 2 represents the density of luminous points which appeared after chemical etching of GaAs substrates [2].

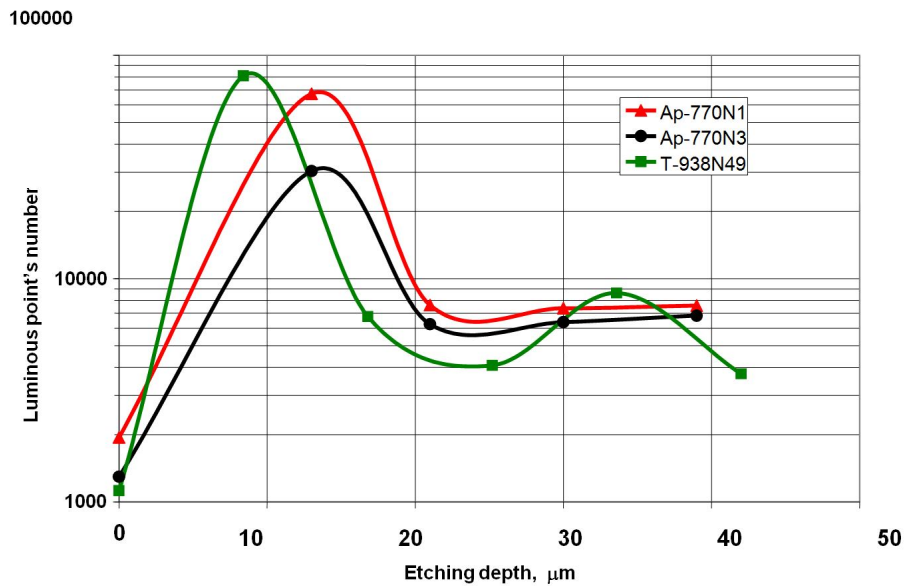


Figure 2. The dependence of number luminous points on etching depth (013) GaAs.

It is clear that the density of luminous point changes with etching depth increases more than one order of magnitude from initial values reaches maximum at 10-15 μm. So we determined the optimal etching depth for epitaxial growth MCT HES which is equal to ~20 μm.

It was determined that carbon contamination does not evaporate at thermal treatment in ultra-high vacuum. The presence of 0,06 monolayer carbons coating on the GaAs surface is disturb epitaxy [3-5]. It necessary to create a continence protective layer more than monolayer thickness which must not adsorbs carbon and desorbs at low temperatures. It was found by SIMS that at treatment of etching GaAs surface in HCl solution in spirit lead to decrease of carbon on the surface less 0.5 % monolayer [6]. At this procedure the arsenic oxides and gallium oxides were removed at room temperature from the GaAs substrate leading to stoichiometric surface with elemental arsenic coating.

We used the procedure of final etching in boiling HCl solution in isopropyl alcohol for formation elemental arsenic coating.

So, the chemical procedure of GaAs surface preparation before the growth includes the etching in H₂SO₄/ H₂O₂/H₂O (3:1:1) mixture at 35-40 °C during 6-10 min. and final and in boiling HCl solution in isopropyl alcohol during 10 min.

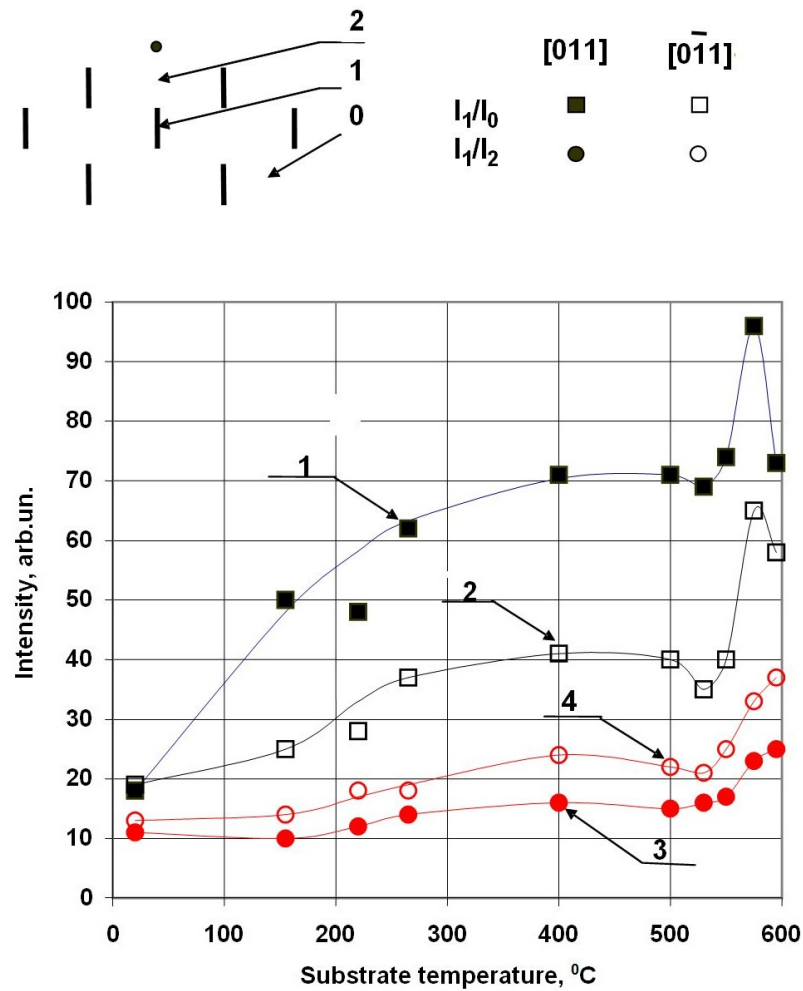


Figure 3. The diffraction reflections intensity dependences on temperature at thermal heating (001)GaAs: curves 1 and 3 in [011] azimuth, curves 2 and 4 in [0 $\bar{1}$ 1] azimuth.

After chemical etching GaAs substrates are attached to special holder and then loaded into loading-unloading vacuum chamber of ultra-high MBE set.

The procedure of thermal heating of GaAs substrate in vacuum are developed using (001) GaAs together with monitoring by high energy electron diffraction (HEED) and single wavelength automatic ellipsometer (AE) LEF-755. Usually before the thermal treatment it is seen weak diffraction pattern from (100)GaAs in [11] and [0 $\bar{1}$ 1] azimuths (weak diffraction reflection). The increasing of brightness of diffraction reflection is observed at increasing temperature GaAs substrate up to 250 ÷ 300 °C. The diffraction background is practically disappeared at temperatures more than 500 °C with appearance diffraction strikes and superstructures 2×1 and 3×1 types.

Fig. 3 showed the typical dependences of diffraction reflection intensity of (100)GaAs surface (curves 1 and 2 for [11] и [0 $\bar{1}$ 1] azimuths) normalized to diffraction background on tem-

perature. The curves 3 and 4 shows the intensity distribution along diffraction strikes in [11] and [011] azimuths respectively. The sharp increasing of diffraction reflection intensity was observed at GaAs substrate thermal heating from 20 °C to 300 °C that connected with desorption of volatile arsenic oxides [1]. The following sharp increasing of diffraction reflection intensity with formation strikes was observed at temperature more 540 °C that means the formation atomic smooth GaAs surface. The further temperature increasing or exposing during 0.5 hour of GaAs substrate 570-580 °C leads to transfer diffraction strikes to diffraction reflections connected with roughening surface.

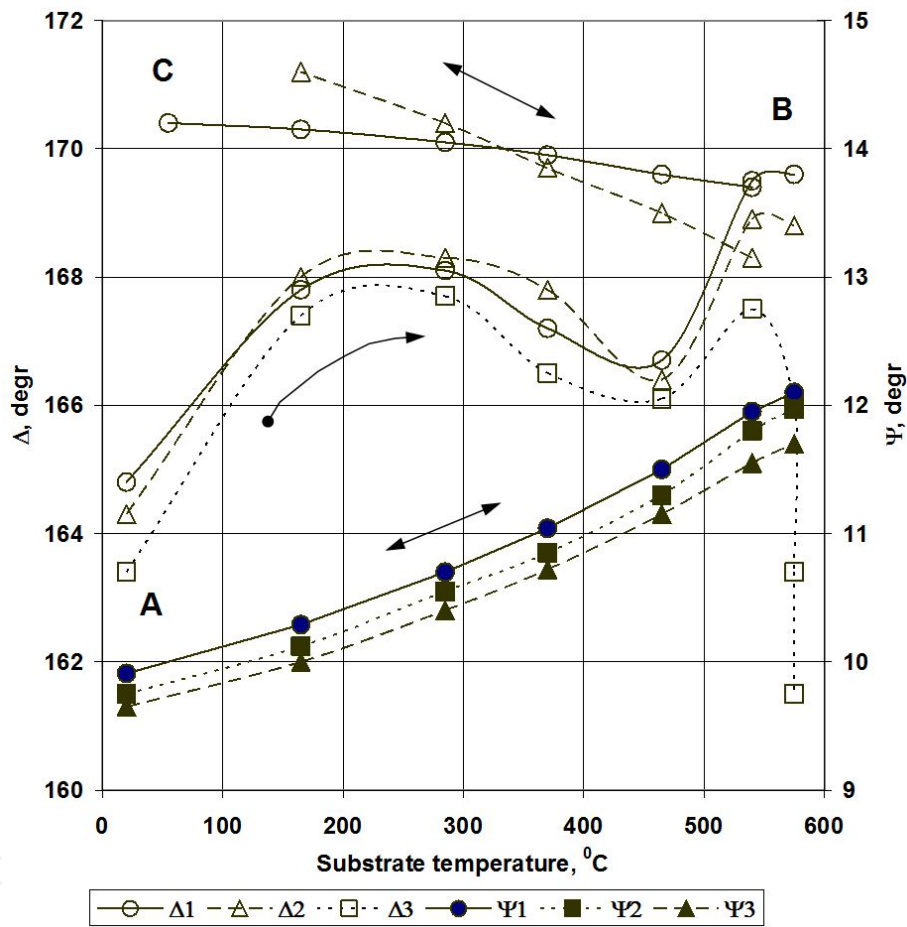


Figure 4. The dependences ψ and Δ on temperature at thermal heating and cooling for 3 samples (001)GaAs. The rows show the direction of changing of ellipsometric parameters.

The typical changing of ellipsometric parameters ψ and Δ were measured at thermal heating (001)GaAs up to 580 °C and cooling to room temperature (see Fig. 4).

The dependence of ψ on substrate temperature showed has reversible character because of that determined by GaAs optical constants. The dependence of Δ on temperature showed non-monotone character that determined by the GaAs surface roughness. The increasing of Δ at thermal heating to ~ 150 °C was conditioned by desorption of adsorbed gases from (001)GaAs surface. Further changing Δ was determined by desorption arsenic oxides [1] and

optical constant temperature dependence. Then we observed the sharp increasing Δ connected with desorption of gallium oxides [1]. The ellipsometric parameter Δ was increased at cooling to room temperature that connected with the changing of GaAs optical constants. The ellipsometric measurements of (001)GaAs surface at thermal treatments are in a good agreements with REED measurements.

These data given the understanding of technological process of preparation atomic smooth and clean (001)GaAs surface by thermal heat treatments. The technological process of preparation (013)GaAs atomic smooth and clean surface is analogous ones. We observed analogous changing of REED pattern and ellipsometric parameters ψ and Δ at thermal heat treatments of (013)GaAs in vacuum.

2.2. The growth of ZnTe/CdTe buffer layer

The buffer layer on (013)GaAs was fabricated by sequence growth of ZnTe and CdTe layers. At first the 20–300 nm ZnTe layer was grown on atomic smooth and clean GaAs surface from separate molecular beam Te₂ and Zn. This procedure is necessary to growth of only one (013) orientation. At CdTe growth on GaAs surface there was observed the growth of mixture orientation [7] that determined with large lattice mismatch 14,6 % between CdTe и GaAs.

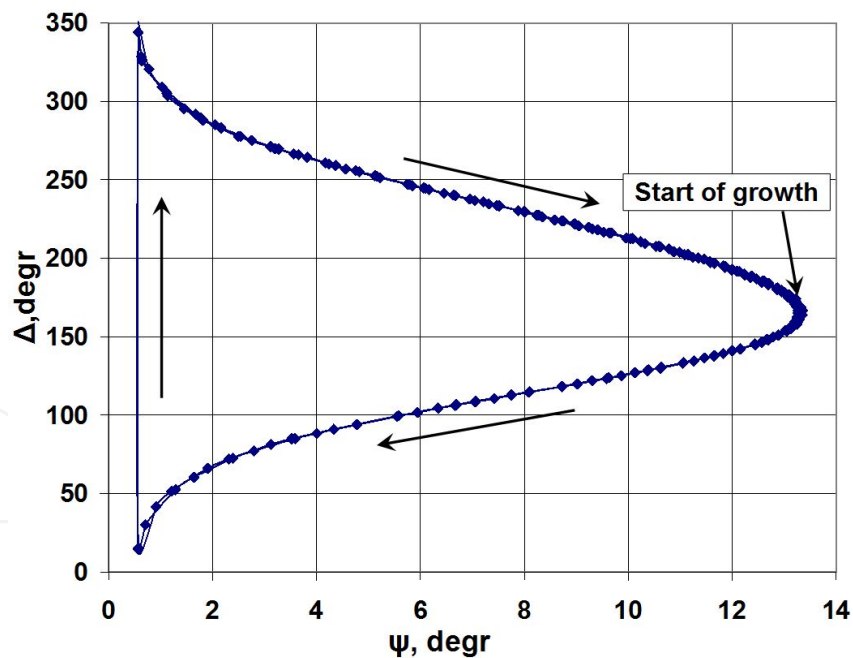


Figure 5. The changing of ellipsometric parameters Ψ and Δ at growth of high quality ZnTe layer at optimal growth conditions. The points – experimental data. The rows show the direction of changing Ψ and Δ at increasing ZnTe thickness.

The optimization of ZnTe growth was carried out with monitoring technological processes by AE *in situ*. At growth of high quality ZnTe in optimal conditions the undamped periodic changing of ellipsometric parameters Ψ and Δ (light radiation AE $\lambda=6328 \text{ \AA}$) are observed

that determined by interference with period $d_0 = \frac{\lambda}{2\sqrt{n^2 - \sin^2\phi}}$ where n – refractive index of ZnTe, ϕ - angle of incidence of AE laser beam on GaAs surface (see Fig. 5).

The deviation from optimal conditions leads to surface roughness or adsorption to changing optical constants because of inclusion in layer volume at ZnTe growth.

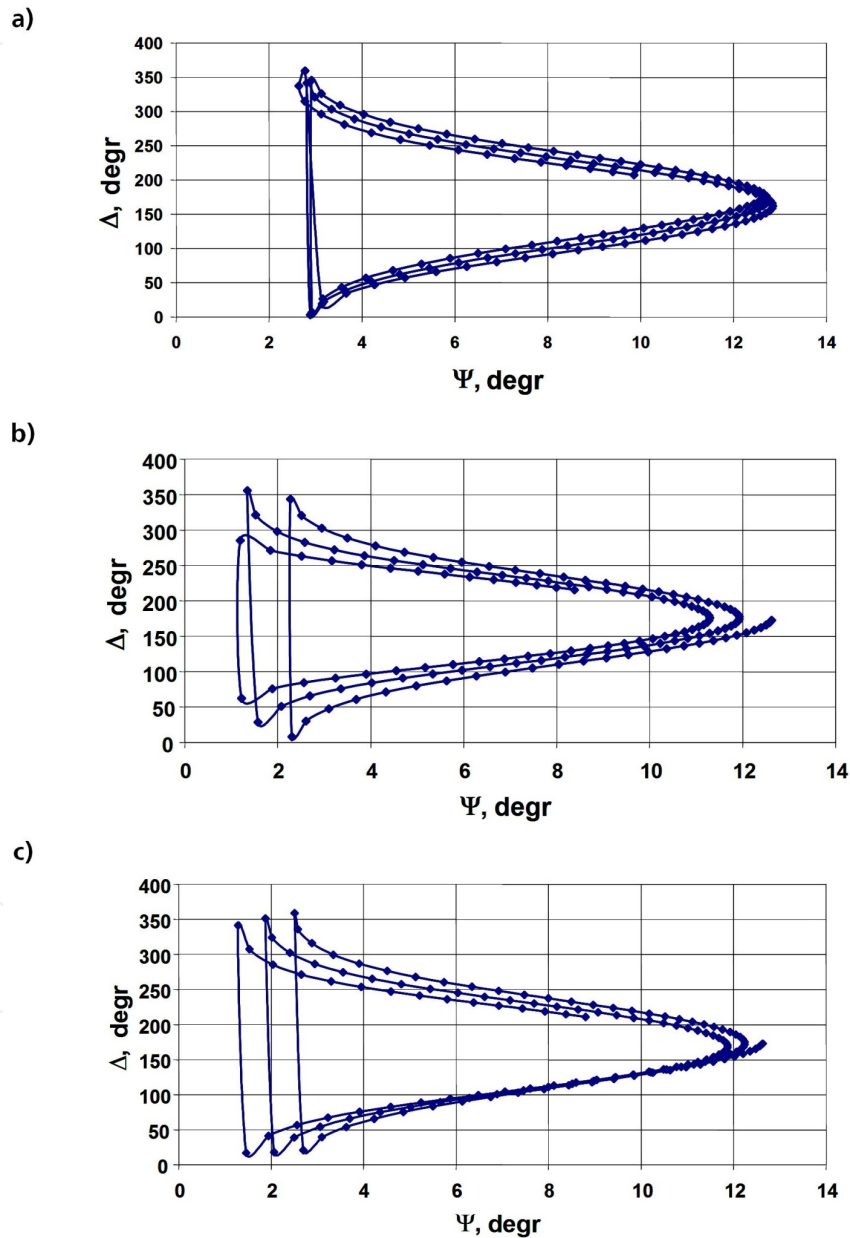


Figure 6. The calculation data of changing of ellipsometric parameters Ψ и Δ at ZnTe growth on GaAs: a – roughness changes from 0 nm up to 5 nm A; b – absorption factor $k=0.05$; c – roughness changes from 0 nm up to 2,5 nm, absorption factor $k=0.03$.

Fig. 6 shows the results of calculations of changing of ellipsometric parameters Ψ and Δ at surface roughness and changing optical constants. The ellipsometric variation of Ψ and Δ in Ψ - Δ plane is little by little move to decreasing Δ at relief evolution (see Fig.6 a). The ellipsometric curve amplitude is decreased at growth of weakly adsorption layer c $k=0,05$ (see Fig. 6b). Fig. 6c shows the changing of Ψ и Δ at developing roughness and absorption factor (k) of growing ZnTe layer.

These data were used for determination of growth mechanism ZnTe on (013) GaAs at growth conditions. The behavior of ellipsometric parameters Ψ and Δ at 2 D and 3D growth is similar as shown in Fig. 6a and Fig. 6b respectively.

Fig. 7 represents the experimental data of the ZnTe growth on (013) GaAs at different temperatures and different molecular fluxes of zinc and tellurium (J_{Zn}/J_{Te2}).

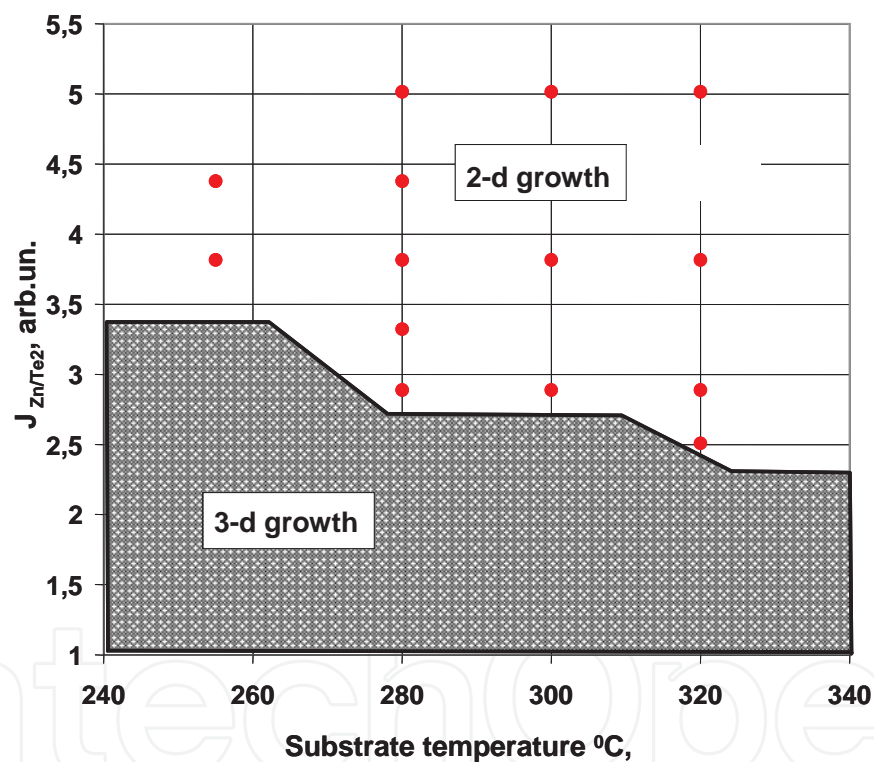


Figure 7. The phase diagram of ZnTe growth mechanism: triangular – 2D growth; points – 3 D growth; solid curve – the boundary of growth conditions between 2D and 3 D growth.

Following these data we determined the optimal conditions for growth of high quality ZnTe layer on GaAs. The temperature of substrate is situated in range 280°C - 295°C at molecular fluxes relations J_{Zn}/J_{Te2} in range 3 - 8.

The studies of CdTe growth on (001) and (013)ZnTe/GaAs substrates were carried out with monitoring by AE *in situ*. Fig. 8 shows the spiral variation of experimental and calculated ellipsometric parameters Ψ and Δ in Ψ - Δ plane at CdTe growth on (001) GaAs.

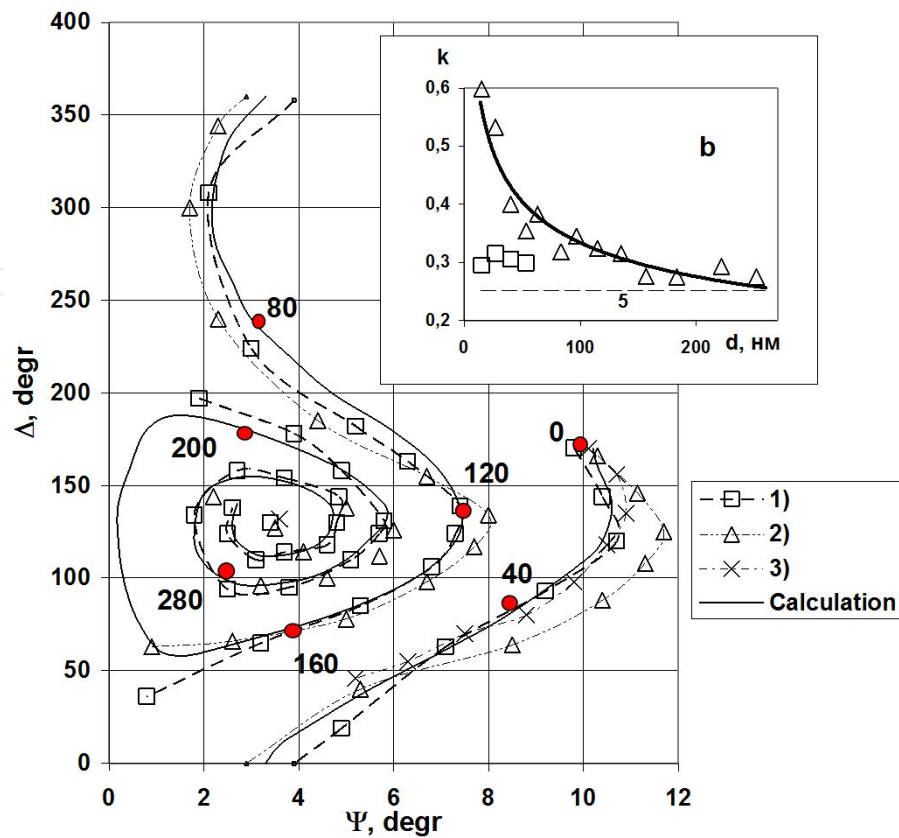


Figure 8. The variation of ellipsometric parameters Ψ и Δ at CdTe growth (001)GaAs for 3 samples: squares, triangular and crosses– experimental data; solid lines – calculation data. Figures near curves – CdTe layer thickness. In insert – the dependence of adsorption factor on thickness for case of essential differences (triangular) and good agreement (squares) between experiment and calculation respectively.

In case of good agreement of experimental and calculated data Ψ and Δ (curves 1 and 3) allows to determine the growth rate and the thickness of growing CdTe layer.

The differences of experimental and calculated Ψ and Δ data at initial stage (up to 200 nm) we observed at growth at non optimal growth condition (curve 2). REED pattern shows the presence of (001) and (111) orientation. At further growth the experimental and calculated Ψ and Δ data becomes near one another.

The observed differences of experimental and calculated Ψ and Δ data свидетельствуют, that optical constants of CdTe for this case are differed from analogous data for bulk CdTe. Really the calculation (see Fig. 8 in insert triangular) shows that adsorption coefficient higher at initial growth stage and reached the bulk data at thickness 200 nm. The higher values of k are explained by poor crystalline performance at initial stage of CdTe on GaAs [8]. Refractive index $n = 3$ does not depend on growth condition of CdTe growth. These studies determined necessity of ZnTe growth on GaAs before CdTe growth.

The optimal conditions for growth of high quality CdTe on (013)ZnTe/GaAs substrate were determined during investigation of technological processes at different growth temperature and molecular cadmium and tellurium fluxes (J_{Cd}/J_{Te2}) relationships with monitoring by AE *in situ*.

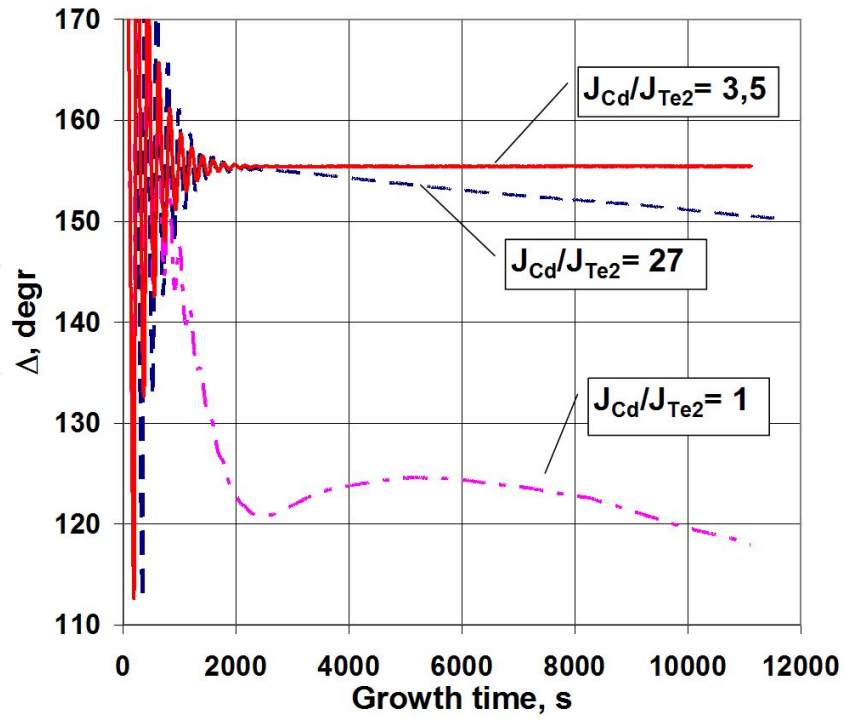


Figure 9. The changing of ellipsometric parameter Δ at CdTe growth.

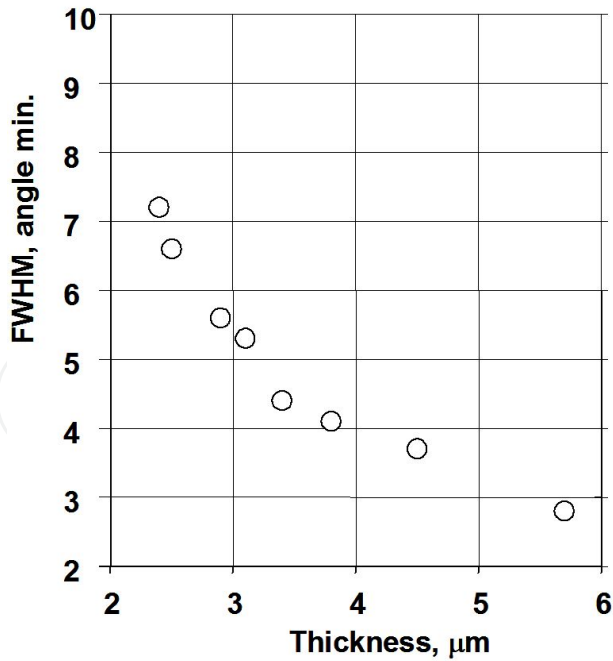


Figure 10. The dependence of FWHM on CdTe thickness.

Fig. 9 represents the changing of ellipsometric parameter Δ at CdTe growth at temperature 290°C and constant molecular tellurium flux. The ellipsometric parameter Δ practically does

not changed at stationary stage of CdTe growth at $J_{\text{Cd}}/J_{\text{Te2}} = 3,5$. A large excess of cadmium at $J_{\text{Cd}}/J_{\text{Te2}} = 27$ it was observed weak decreasing of ellipsometric parameter Δ . In condition of stoichiometric relationship $J_{\text{Cd}}/J_{\text{Te2}}=1$ it was observed sharp decreasing of ellipsometric parameter Δ that determined by sharp surface roughening.

It well-known that a large dislocation density in CdTe/ZnTe interface [9] was formed and decreased with increasing of CdTe thickness [10]. The growth of CdTe layers with different thickness were carried out at optimal condition. Fig. 10 shows the dependence of full width of half maximum (FWHM) of rocking curves on CdTe layer thickness.

It is clear that FWHM sharply decreased at increasing of CdTe thickness reaching practically stationary values less 3 angle minutes at 6 μm .

So we determined the optimal conditions for growth of high quality CdTe layer on (013)ZnTe/GaAs. The temperature of substrate is situated in range 280°C - 295°C at molecular fluxes relations $J_{\text{Cd}}/J_{\text{Te2}}$ in range 5 - 7. The thickness of CdTe layer is 5 – 7 μm .

The AFM measurements showed that grown CdTe surface roughness less than 10 nm.

2.3. The growth of MCT layers

The growth of MCT layer was carried out on (013)CdTe/ZnTe/GaAs substrates from separate molecular sources of elemental Cd, Te и Hg. The original construction of molecular sources and their unique location in vacuum chamber allows to grow MCT layer with high uniformity over the surface area of 3" in diameter GaAs substrate without rotation (see Fig. 11).

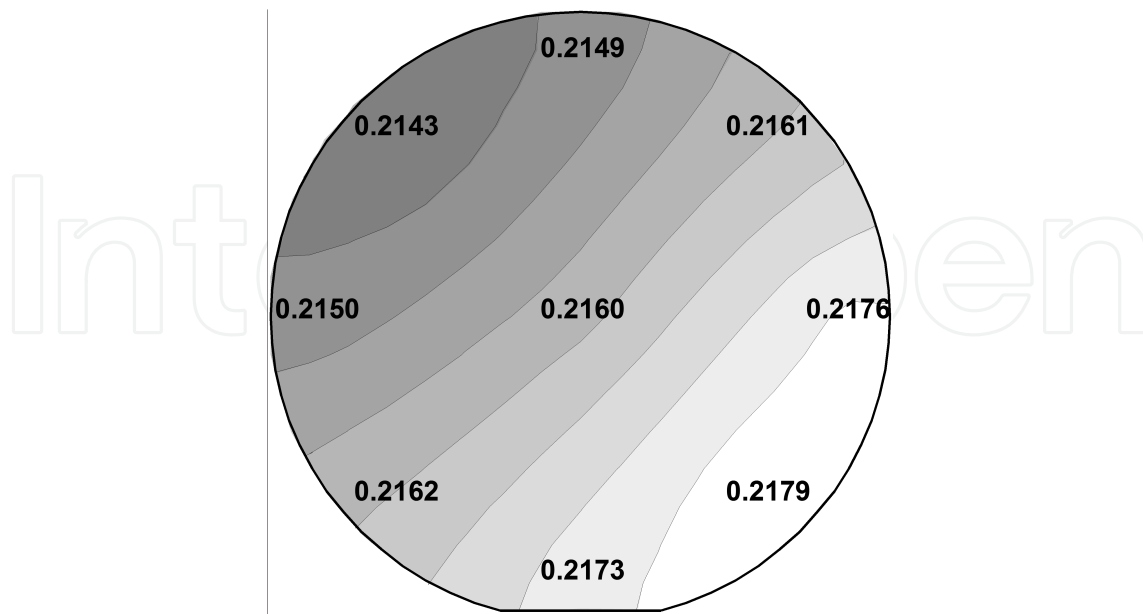


Figure 11. The MCT composition uniformity over the surface area of 3" in diameter GaAs substrate measured by transmission spectra. The mean value $\langle X_{\text{CdTe}} \rangle = 0.2164$ and standard deviation $\delta \langle X_{\text{CdTe}} \rangle = 0,0036$.

It is clear that MCT composition mean value $\langle X_{\text{CdTe}} \rangle = 0.2164$ and standard deviation $\delta \langle X_{\text{CdTe}} \rangle = 0.0036$. So during the growth of MCT layer we used for monitoring technological process AE *in situ*.

It is necessary to remark that the MCT growth conditions differ from molecular regime. There is exist high mercury pressure $10^{-3} - 10^{-4}$ torr at growth MCT layer because low sticking coefficient. The tellurium adsorbed on the growth surface as diatomic molecules with formation solid phase MCT through reaction with cadmium and mercury. There is the possibility to formation solid phase of tellurium at growth temperatures 185-190 °C for case of mercury deficit for some reasons. The thermodynamic analysis reveals the possibility of existing two solid phases – MCT and tellurium. Consequently, the processes on the growing surface determined by crystallization tellurium with formation of high quality MCT layer or solid phase of tellurium which leads to defect structure [11,12]. So we determined the optimal growth condition with the purpose to decrease appearance defects as minimal as possible. In opposite case there is possibility of irreversible decreasing of surface roughness and crystalline perfection of epitaxial structure.

At initial stage of MCT growth the changing of ellipsometric parameters Ψ and Δ in Ψ - Δ plane represents by convergent spiral curve (Fig. 12).

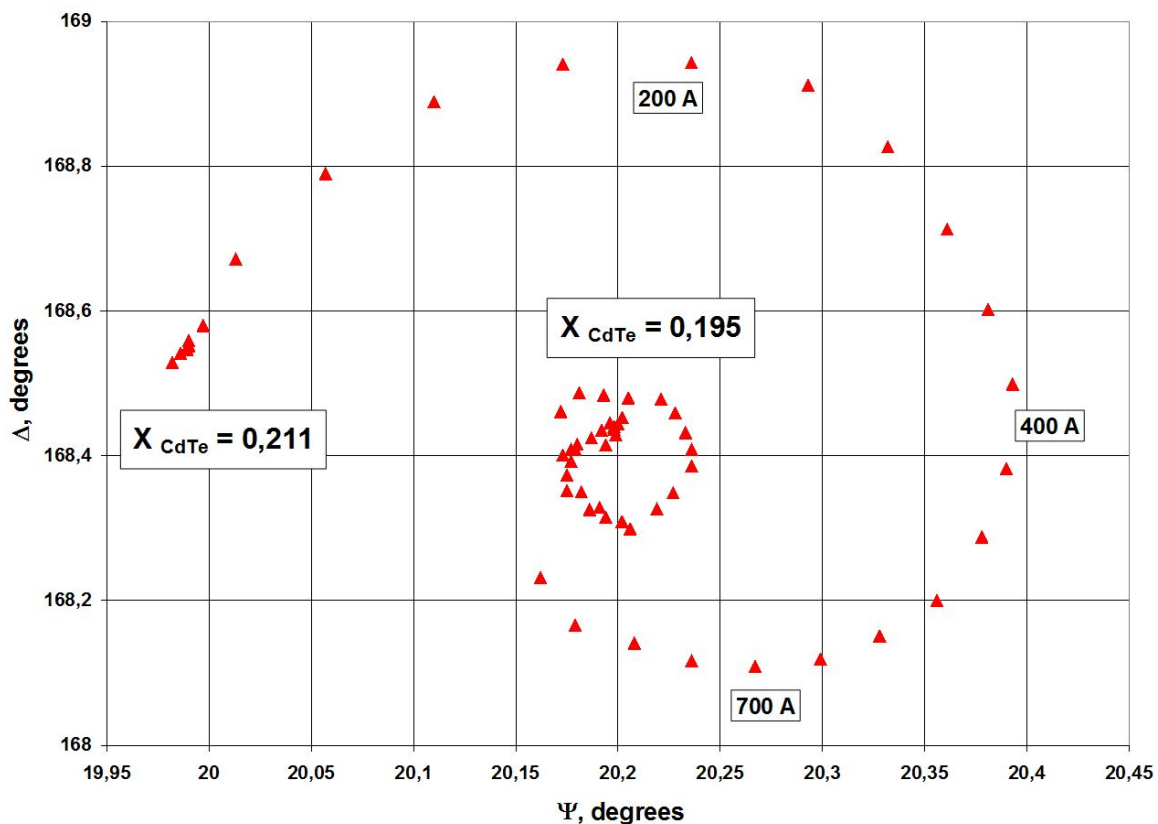


Figure 12. The evolution of ellipsometric parameters Ψ and Δ in Ψ - Δ plane at initial stage of growth: triangular – experimental data; dotted line – calculated data. The цифры – MCT thickness.

This dependence allows to determine the growth rate and MCT composition. These data allows in further to provide monitoring of MCT thickness and MCT composition and its changing at stationary growth stage *in situ*. Note that (013) substrate orientation is appropriate for MCT layer growth of different composition without essential changing technological conditions. This circumstance allows to grow MCT HES with special design to improve the parameters of detectors and to simplify their technological process of fabrication.

Fig. 13 shows the MCT HES in which there is graded wide gap layer on the boundaries of absorber layer. Widegap layers created built-in electric fields in which non-equilibrium carrier's drive back into the volume from surfaces with high recombination velocities and acted as passivating coatings. Wide gap layers lead to the essential increase of minority lifetime. In insert it is shown the variation of growth temperature measured by polarized pyrometer. It is seen that the variation of growth temperature lies in interval 186 -188 °C that gives the variation of MCT composition less than 0,001 mole fraction of CdTe. This data were supported by measurement of transmission spectra with layer-by-layer chemical etching which in a good agreement with ellipsometric measurement of MCT composition *in situ*.

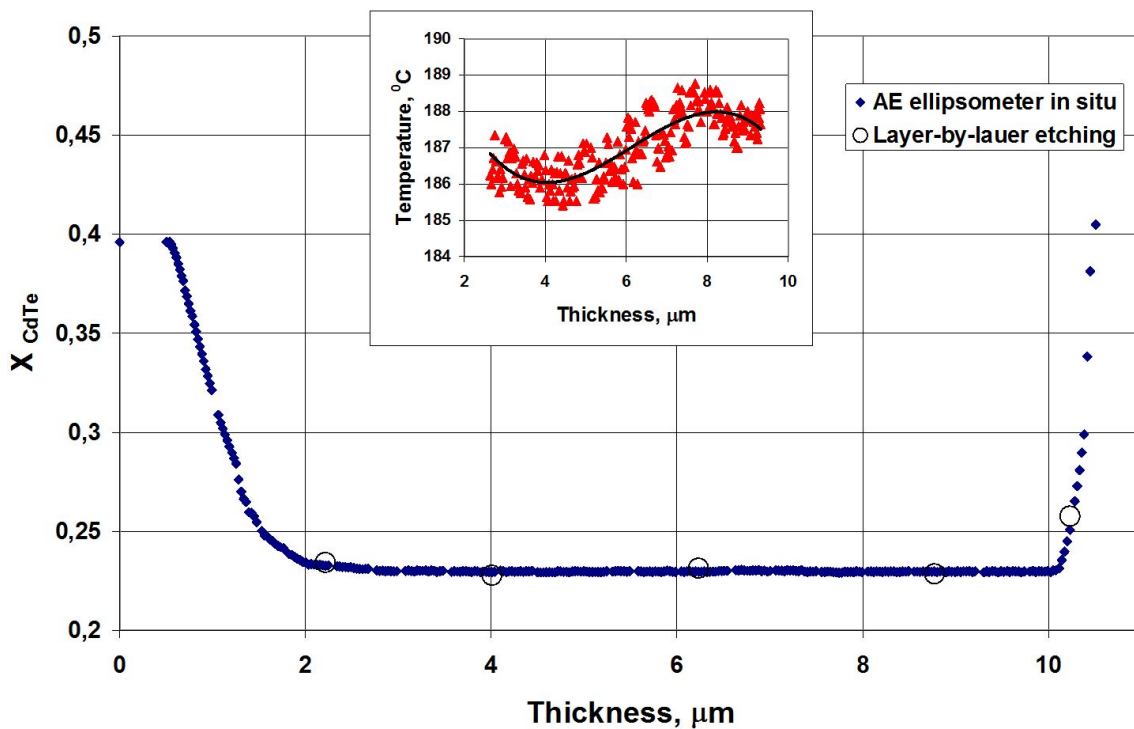


Figure 13. The distribution of MCT composition throughout the thickness measured by AE *in situ*. Open circles – MCT composition measured by transmission spectra at layer-by-layer chemical etching. In insert – variation of growth temperature during MCT growth.

We suggested the novel MCT HES allows to decide the problem of high sequence resistance for matrix focal plane arrays (FPA) based on p-type absorber layer.

The construction of absorber layer for p-type MCT HES used for matrix photovoltaic (PV) FPA includes additional MCT layer with high conductivity. The additional MCT layer with

high conductivity must be fabricate by intentional doping of more wide gap layer or growing more narrow layer than absorber ones during the growth MCT HES.

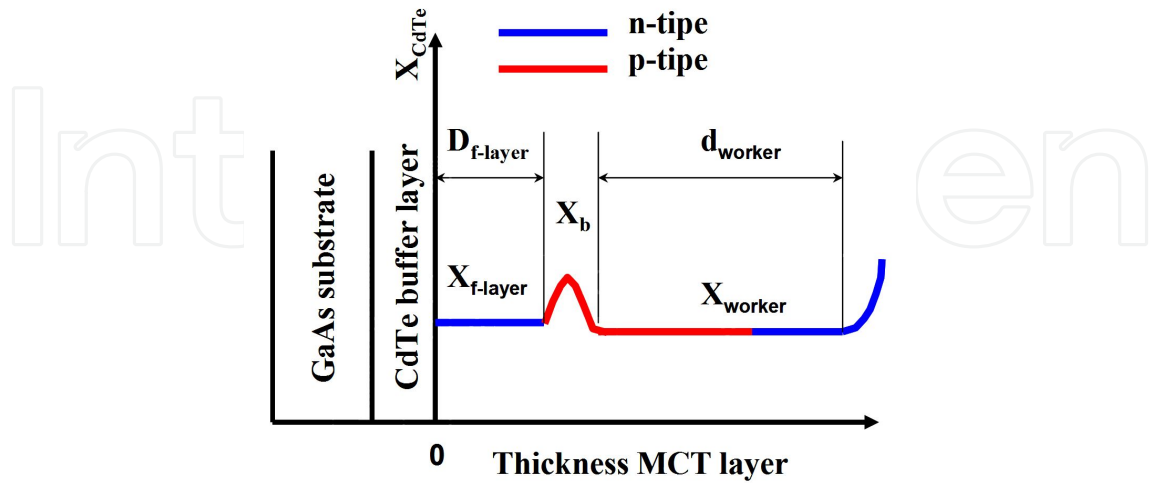


Figure 14. Novel construction of MCT HES for matrix PV FPA.

Fig. 14 shows the MCT composition distribution throughout the thickness for novel MCT HES for large format matrix PV FPA.

MCT HES includes the following layer which is growing in sequence technological process:

- the high conductivity layer n-type with In doping up to more than $n=5 \cdot 10^{16} \text{cm}^{-3}$;
- the barrier excluded cross-talking between high conductivity layer and absorber ones;
- graded wide gap layers on the boundaries of absorber layer.

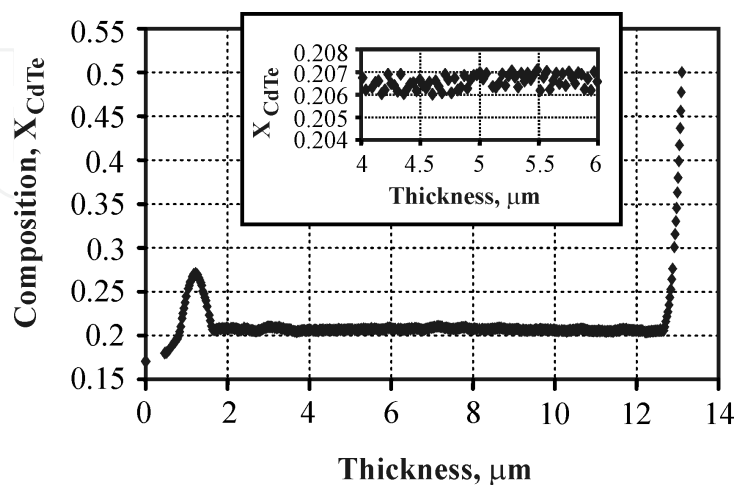


Figure 15. MCT composition profile throughout the thickness with narrowgap+widegap layer at the interface and widegap at the surface measured by AE *in situ*. In insert – variation of MCT composition in MCT volume.

The MCT composition in this layer is slightly more than for absorber layer. These high conductivity layer decreases of sequence resistance and serves as short wavelength cut off filter for cooling PV FPA. It was determined by photoconductive measurement the minimal height of barrier layer 0,05 mole fraction CdTe. Fig. 15 illustrates a novel MCT HES MBE with variation of MCT composition on boundaries of absorber layer. In Fig. 15 the MCT composition profile with narrowgap layers at the interface and widegap layer at the surface is shown. There is a barrier layer as wide gap layer between narrowgap and absorber layers. Narrowgap layer sharply decreases diodes series resistance.

2.4. Electrical parameters MCT HES

Electrical characteristics were determined from Hall measurements at 77 K by Van der Paw method. As grown MCT HES MBE with construction represented in Fig. 12 had n-type conductivity. The electron concentration and mobility and minority carrier lifetime were 10^{14} - 10^{15} cm^{-3} and over 10^5 $\text{cm}^2/\text{V sec}$ and 2-10 μs for composition $X_{\text{CdTe}} \sim 0,20$ - $0,22$ respectively. For conversion of as-grown n-type MCT HS's MBE to p-type annealing in helium atmosphere was carried out at 200-250°C and low mercury vapor pressure. After annealing hole concentration and mobility were $(5 - 20) \times 10^{15}$ cm^{-3} and 400 - 700 $\text{cm}^2/\text{V s}$ for composition $X_{\text{CdTe}} \sim 0,20$ - $0,22$.

3. The design and parameters IR detectors

3.1. The graded widegap layer at the boundaries of MCT absorber layer

The graded widegap layer at the boundaries of MCT absorber layer allows to improve IR detectors and simplify the technology of their development and fabrication.

We studied the influence of widegap layers at the boundaries of absorber layer on minority lifetime by numerical calculation and supported this effect by experimental investigations.

The distribution of non-equilibrium carrier was determined by decision of one dimensional diffusion equation taking into account the generation-recombination processes and built-in electric in graded widegap layer. The dependence of hole current j_p on the thickness position y in homogeneous MCT n-type in approximation of low generation expressed by following [13]:

$$j_p(y) = \mu_p(y)p(y)k_B T \frac{d}{dy} \ln n_i^2(y) - \mu_p(y)k_B T \frac{d}{dy} p(y) \quad (1)$$

where μ_p - hole mobility, p - carrier concentration, n_i - intrinsic carrier concentration, T - temperature, k_B - Boltzmann constant.

The equation of non-equilibrium hole in MCT n-type expresses by

$$\frac{k_B T}{e} \frac{d}{dy} j_p(y) - G(y) + \frac{p(y) - p_o(y)}{\tau(y)} = 0 \quad (2)$$

where e – electron charge, p_o – equilibrium hole concentration. The generation rate is expressed by equation

$$G(y) = \alpha(y) F \exp\left(-\int_0^y \alpha(y') dy'\right) \quad (3)$$

where F - photon flux of radiation, α - absorption factor, τ - the recombination time of charge carriers. At homogeneous MCT composition this time τ_A is determined by Auger processes $A1$ [14]. For calculation of recombination time τ_d limited by dislocation density n_d we used the expression of empirical model [15]:

$$\tau_d = \frac{C_d}{n_d} \quad (4)$$

where C_d – fitting parameter depended chemical composition of semiconductor, technology of fabrication and dislocation nature.

So the recombination time in (2) is determined by expression:

$$\frac{1}{\tau} = \frac{1}{\tau_A} + \frac{1}{\tau_d} \quad (5)$$

The boundary conditions are expressed by [11]:

$$j_p(0) = -es_o[p(0) - p_o(0)], \quad j_p(L) = es_L[p(L) - p_o(L)] \quad (6)$$

where L - MCT layer thickness, s_o, s_L – the recombination velocity at interface $y=0$ and at the surface $y=L$ of MCR absorber layer.

The equation 2 is decided by difference method. Further the effective lifetime τ_{eff} is determined from the following equation through the non-equilibrium carrier Δp as:

$$\tau_{eff} \int_0^L G(y) dy = \int_0^L \Delta p(y) dy \quad (7)$$

The calculations were done for photoconductor fabricated on basis of MCT HES with MCT distribution throughout the thickness represented in Fig. 12. The thickness of absorber layer and widegap layers is equal to $L=10$ and $1 \mu\text{m}$ respectively. The MCT composition in absorber-

er layer is $x_{CdTe} = 0.2$. The MCT composition on the surface is varied. The electron concentration is $n = 4 \cdot 10^{14} \text{ cm}^{-3}$ at 77 K. The surface recombination velocity at interface with CdTe and at the MCT surface is $s_0 = 10^5 \text{ cm/c}$ and $s = (0 - 10^7 \text{ cm/c})$. We measured the dislocation densities and lifetime in 2-x MCT HES for C_d determination. We calculate using (4) $C_d = 40\text{-}80 \text{ c/cm}^2$ at measured n_d (4 -6) 10^7 cm^{-2} and lifetime 0.4-0.8 μs .

Follow τ_{eff} calculation we found that the graded widegap layer leads to decrease of the influence of surface recombination because of existing built-in electrical field (see Fig. 16).

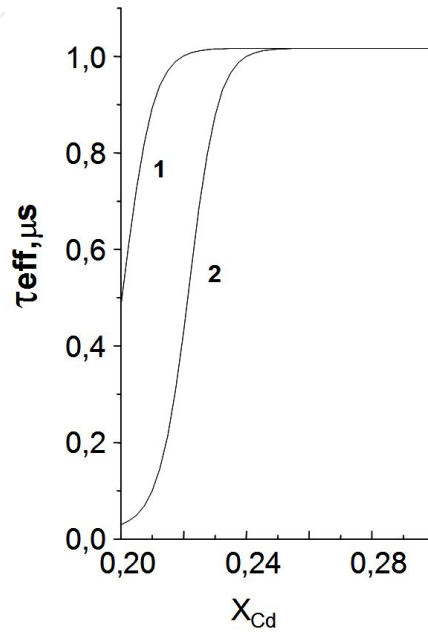


Figure 16. The effective lifetime τ_{eff} in MCT HES. The dislocation density- $5 \cdot 10^7 \text{ cm}^{-2}$, $C_d = 60 \text{ s/cm}^2$. The surface recombination velocity: 1 - 10^3 cm/s , 2 - 10^5 cm/s .

It is needed only $\Delta x_{Cd} = x_{Cd}^s - x_{Cd}^b = 0.05$ for suppression of surface recombination which compared to analogous ones in [16].

We compared the calculated lifetime τ_{calc} and experimental lifetime τ_{exp} at 77 K measured by photoconductive relaxation in MCT HES with graded widegap layers (Table 1).

Sample	n $\times 10^{14} \text{ cm}^{-3}$	τ_{exp} μs	τ_{calc} μs	n_d^{opt} $\times 10^7 \text{ cm}^{-2}$
1	3.8	1.4	1.4	4
2	2.5	1.1	1.4	5.3
3	8.6	1.2	0.9	2.3
4	1.3	0.75	1.5	8

Table 1.

Here τ_{exp} – experimental lifetime and τ_{calc} - calculated lifetime determined by Auger and dislocation recombination lifetime for $C_d=60$ c/cm² и $n_d=4 \cdot 10^7$ cm⁻². n_d^{opt} - fitting dislocation density for calculated and experimental data lifetime. It is apparently clear a good agreement between calculated and experimental lifetime.

Fig. 17 demonstrates the calculation of changing lifetime at etching layer-by-layer upper graded widegap layer at the surface MCT HES. It is seen that τ_{eff} sharply decreases at completely moving graded widegap layer from the surface.

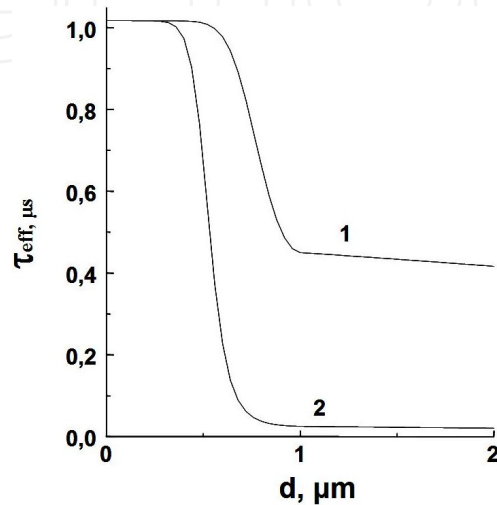


Figure 17. The changing of effective lifetime τ_{eff} on etching graded wide gap layer thickness d for MCT HES: $x_{Cd}^s = 0.3$, $n_d = 5 \cdot 10^7$ cm⁻². The surface recombination velocity: 1 - 10^3 cm/s, 2 - 10^5 cm/s.

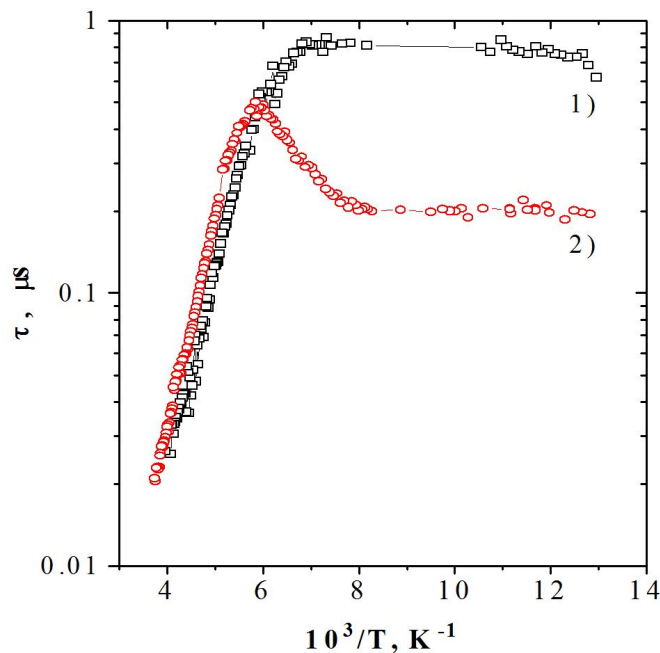


Figure 18. The temperature dependences of lifetime for n-type MCT HES with MCT composition in absorber layer 0,215 mole fraction CdTe: 1) – with graded wide gap layers; 2) – after chemical moving of upper graded wide gap layer.

The testing of influence of graded widegap layers on lifetime was checked experimentally at measurement non contact super high frequency conductivity relaxation before and after chemical etching moving of upper graded widegap layer. Fig. 16 represents the temperature dependences of MCT HES with graded widegap layers at the boundaries of absorber layers (curve 1) and after chemical etching of upper graded widegap layer (curve 2). One can see that the experimental data of measurement lifetime supported the calculation ones at temperatures lower than 150K. It means that the presence of graded widegap layers at boundaries of absorber layer is very important for cooled IR detectors.

3.2. Surface leakage

One important spurious component of p-n junction dark current is leakage current (LC) which limited the threshold characteristics. At low carrier concentration inside p-n junction volume LC current is mainly the surface LC determined by the carrier generation-recombination, tunneling, ohmic conductivity and etc. The surface LC can be expressed by the following equation [17]:

$$I = I_s[\exp q(V-IR_s)/\beta kT) + 1] + (V-IR_s)/R_{sh} + I_T \quad (8)$$

where I_s – saturation current; R_s – sequence resistance; R_{sh} – shunt resistance; V – bias voltage; $I_T \sim \exp[-4(2m)^{1/2}E_g^{3/2}/3q\hbar E]$ for triangular potential barrier; $\beta = 1$ at diffusion current (DC) component $I_D \sim n_i^2 \sim \exp(-E_g/kT)$; $\beta = 2$ at generation-recombination current ((G-R)C) component $I_{GR} \sim n_i \sim \exp(-E_g/2kT)$; E_g – band gap; k – Boltzmann constant; T – temperature.

It is clear that DC or/and (G-R)C decrease exponentially with E_g and falls 10^8 and 10^5 times respectively yet in case of changing of MCT composition from $X_{CdTe} = 0.22$ up to $X_{CdTe} = 0.3$. It means that the presence of widegap layers at the boundaries of active layer suppress effectively surface LC. It is necessary to notice that these widegap layers eliminate the influence of surface on minority lifetime as remembered earlier.

3.3. The role of high conductivity layer in MCT HES

Sequence resistance (R_s) is other parameter which influence on p-n characteristics and determine the IR detector operating frequency range, operating point of heterodyne IR detector and analogous ones of different pixels of FPA etc. In last case it is equivalent of increasing of cross-taking and noise current. Really, R_s reaches several units (MWIR) or tens kilo-ohms (LWIR) for IRD with p-type MCT absorber layer with optimal values $p_{77K} \leq 10^{16} \text{ cm}^{-3}$, $\mu_{77K} = 400\text{-}600 \text{ cm}^2/\text{B}\times\text{c}$ and thicknesses less than $10 \text{ }\mu\text{m}$ and pixel size $20\text{-}40 \text{ }\mu\text{m}$. We suggested decreasing R_s due to narrow gap layer at the interface between absorber and buffer layers of MCT HES. But the presence only narrow gap layer leads to decreasing of quantum efficiency (QE). This problem was solved by the special MCT composition with the growing sequent narrow gap and wide gap layers at interface (Fig. 14). The numerical calculation of QE for different MCT composition distribution at the interface and with wide gap layer at the surface (Fig. 19) was carried out [18,19].

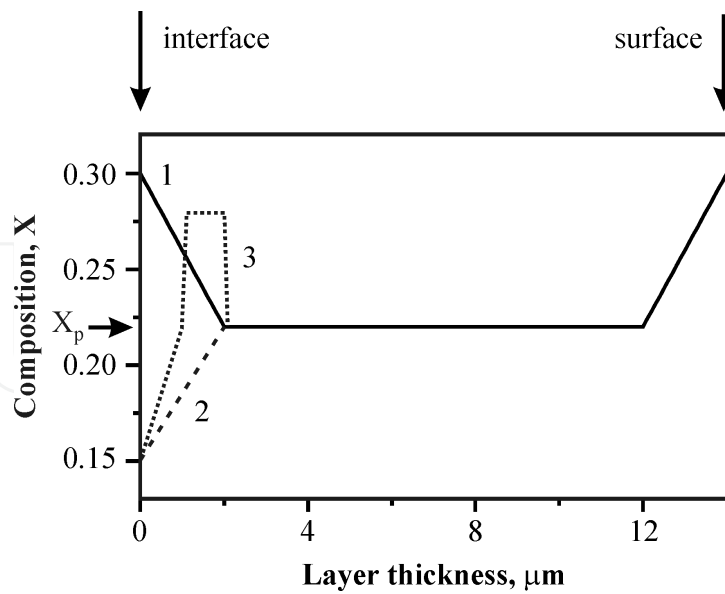


Figure 19. MCT composition (X) distribution throughout the thickness with graded widegap layer at the surface and different layer at the interface: type 1 – widegap (solid line); type 2 – narrowgap (dotted line); type 3 – narrow gap + widegap (pointed line).

The calculated A/W sensitivities (S_j) normalized to λ_{co} is presented in Fig. 19.

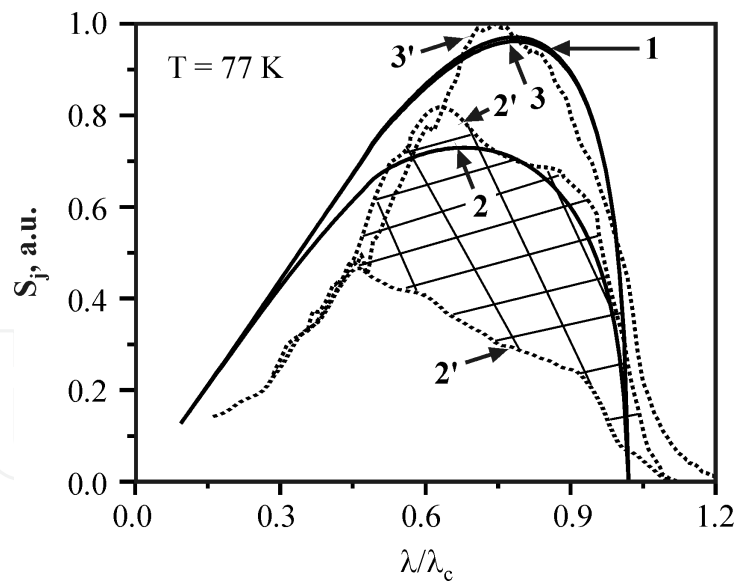


Figure 20. The calculated (solid 1,2,3) and experimental (dashed 1',2', 3') A-W of diodes sensitivity (S_j) normalized to λ_c . Numerals are mean number MCT type on fig.19. Crosshatched region is deviation for type 2.

Apparently clear essential decreasing S_j for MCT HES type 2 especially near λ_{co} in comparing with MCT HES's type 1 and type 3. We fabricated testing diodes on the basis of three types MCT HES and measures V-dependences, differential resistances on bias voltage and spectral responses at 77K. The experimental data is in good agreement with calculated ones.

We found that R_s is equal to approximately several Ohms for MCT HS type 3 and at the same time several hundreds Ohms for MCT HS type 3. It means that the presence of narrow +wide gap layer allows to decrease R_s without IRD performance degradation. Really the typical characteristics of photodiodes with maximum wavelength at $\lambda_p = 7 \mu\text{m}$ and cut-off $\lambda_{co} = 9,1 \mu\text{m}$ were as following: $R_s \sim 1 \text{ OM}$, $R_0A=100 \text{ Ohm}\times\text{cm}^2$, $S_{(\lambda_p)} = 3,5 \text{ A/BT}$, $D^* (\lambda_p, 500 \text{ K}, 1200 \text{ Hz}, 1 \text{ Hz})= 6,5\times 10^{11} \text{ cmHz}^{1/2}\text{W}^{-1}$.

As mentions above there is the problem of sequence resistance at developments of different PV type IR detectors.

For IR detector operated at high frequency the limiting frequency is determined by $R_s \times C$, where R_s – sequence resistance and C – p-n junction capacity. For IR FPA n⁺-p type the increasing of hole concentration in absorber layer more $2 \times 10^{16} \text{ cm}^{-3}$ leads to decreasing of threshold diode parameters at forward bias, decreasing electrons diffusion length and correspondingly decreasing of quantum efficiency. The bulk MCT p-type with the thickness $\sim 1 \text{ mm}$ and hole concentration $2 \times 10^{16} \text{ cm}^{-3}$ used for IR PV detectors ($10.6 \mu\text{m}$) operated at frequencies more than 1 GHz and has a high quantum efficiency when MCT provides wavelength cut off more $12 \mu\text{m}$. For MCT HES p-type a sequence resistance is about k Ω unit that at $C \sim 1 - 10 \text{ pF}$ gives receiving radiation at frequencies lower than 1 GHz.

For large format PV FPA it is necessary to create the same condition (the same bias voltage) for central and edge diodes. At high sequence resistance there is the possibility of so called “debiasing substrate” or “boublik” effects that observed by this time for 128×128 PV FPA.

The problem of sharp decreasing of sequence resistance is decided by growing MCT HES with high conductivity layer which does not influence on threshold PV FPA.

The numerical calculation of n⁺-p diodes current of matrix PV FPA based on MCT HES with p-type absorber layer were carried out. For this n⁺-p junction the minority charge carriers (electrons) are collected by p-n junction, while the excess holes moves to base contact at periphery of FPA. The continuity equation of hole current is described by following expression:

$$\frac{\partial p}{\partial t} = G_p - U_p - \frac{1}{q} \nabla \cdot J_p \quad (9)$$

where G_p – generation rate; U_p – recombination velocity (cm^{-3}/s), q – electron charge, J_p – hole current density.

The hole current density is expressed by

$$J_p = q\mu_p pE - qD_p \nabla p \quad (10)$$

where μ_p – hole mobility, p – hole concentration, E – electric intensity, D_p – hole diffusion coefficient.

For 2-D FPA the stationary equation for homogeneous hole current through the thickness d and taking into account $G_p - U_p = J_s / d$ at low generation rate ($\Delta p \ll p$) is described by

$$\frac{d^2\varphi}{dx^2} + \frac{d^2\varphi}{dy^2} = \rho_s J_s \tag{11}$$

where $\varphi(x,y)$ – the potential in absorber layer, ρ_s – surface resistance $\rho_s = 1/q\mu_p p d$.

The surface current density $J_s = I \times N$, where I – diode current; N – density of surface state. For ideal n-p junction the current is expressed by

$$I = I_{ph} + I_s \left(e^{\frac{qV}{kT}} - 1 \right) \tag{12}$$

where I_{ph} – photocurrent; $V = -(\varphi_d - \varphi(x,y))$ and φ_d – potential at diode from multiplexer and boundary condition $\varphi(x,y) = 0$ at the base contact.

Fig 21 shows the calculation data of distribution of diodes current for the case of appearance of positive voltage bias at central part of FPA due to voltage drop because of large summed current in absorber layer.

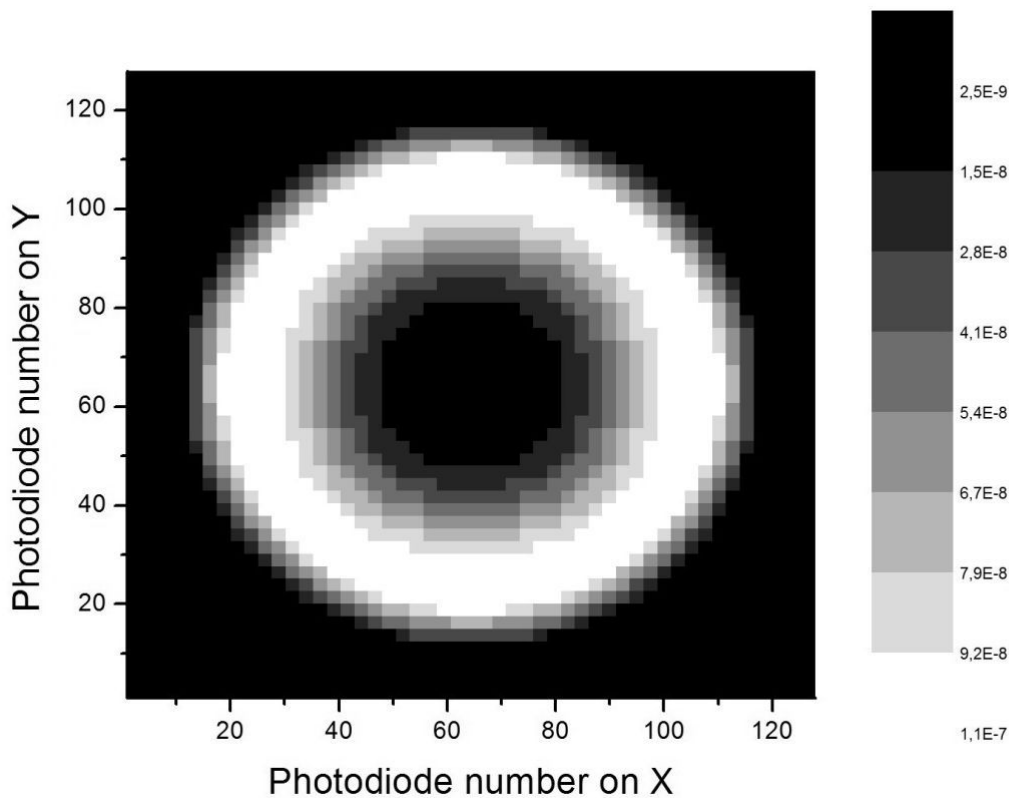


Figure 21. The numerical calculation data of changing of output diodes current at homogeneous radiation of central part of 128x 128 FPA.

This data demonstrates “debiasing substrate” or “boublik” effect which means the breaking of central diodes that observed experimentally (Fig. 22).

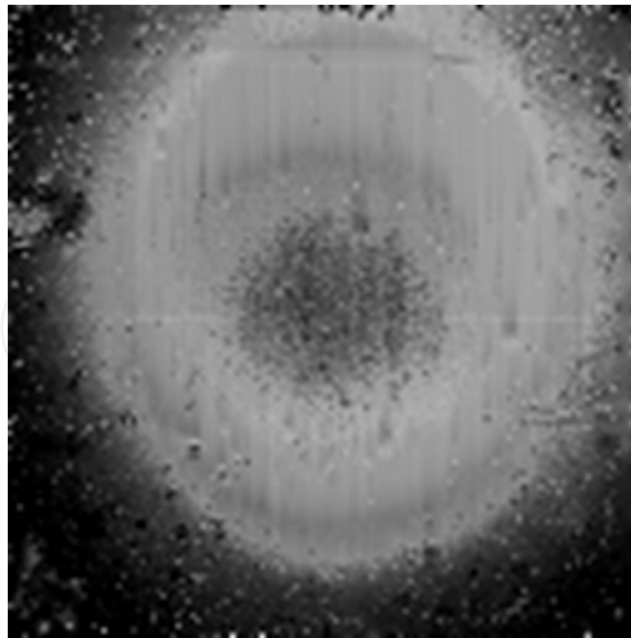


Figure 22. The experimental image at homogeneous radiation of central part of 128× 128 PV FPA n-p type.

For decreasing or elimination of “debiasing substrate” or “boublik” effect we suggested high level doping (Fig. 14) or narrow gap layer (Fig. 15) during growing MCT HES.

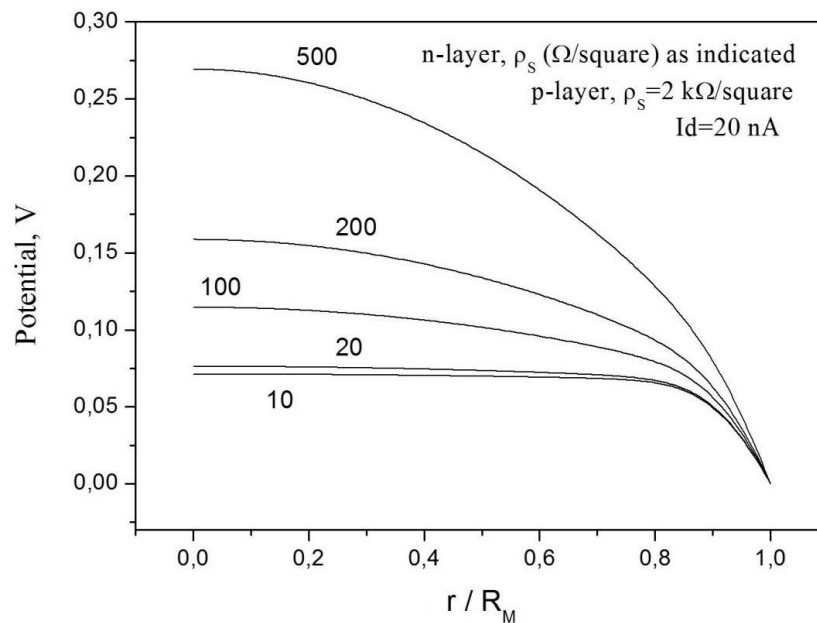


Figure 23. The numerical calculation data of potential distribution in 640×512 PV FPA p-type on dependence of resistance of high conductivity layer. The photocurrent of diodes is 20 nA.

In case of fabricating high conductivity layer by doping during the growth the thickness d and MCT composition can be chosen for creating cooled short wavelength cut off filter.

The results of numerical calculation of potential distribution in the absorber layer for 640×512 PV FPA is shown in Fig. 23 with the following parameters: $I_d = 20$ nA; $A = 6.25 \times 10^{-6}$ cm²; $\rho_s = 2$ kΩ/□ ($p = 8 \times 10^{15}$ cm⁻³, $\mu_p = 400$ cm²/(V×s); $d = 10$ μm); n - p junction between n -type layer and barrier layer is ideal with the density of saturation current $J_s = 1.6 \times 10^{-7}$ A/cm²; ground potential to base contact.

The good values of voltage drop lower 70-110 mV reached at resistance 10-100 Ω/□ of high conductivity layer thickness 3 μm doping by In up to $(1-5) \times 10^{16}$ cm⁻³.

3.3. MCT HES p-P design

The special dual layer absorber construction of MCT HES p-P type (p in narrowgap part of absorber layer; P in widegap of absorber layer) (see Fig.24) allows to decrease dark current and photocurrent that leads to increase of wavelength cut off in range 8-12 μm or operating temperature [20].

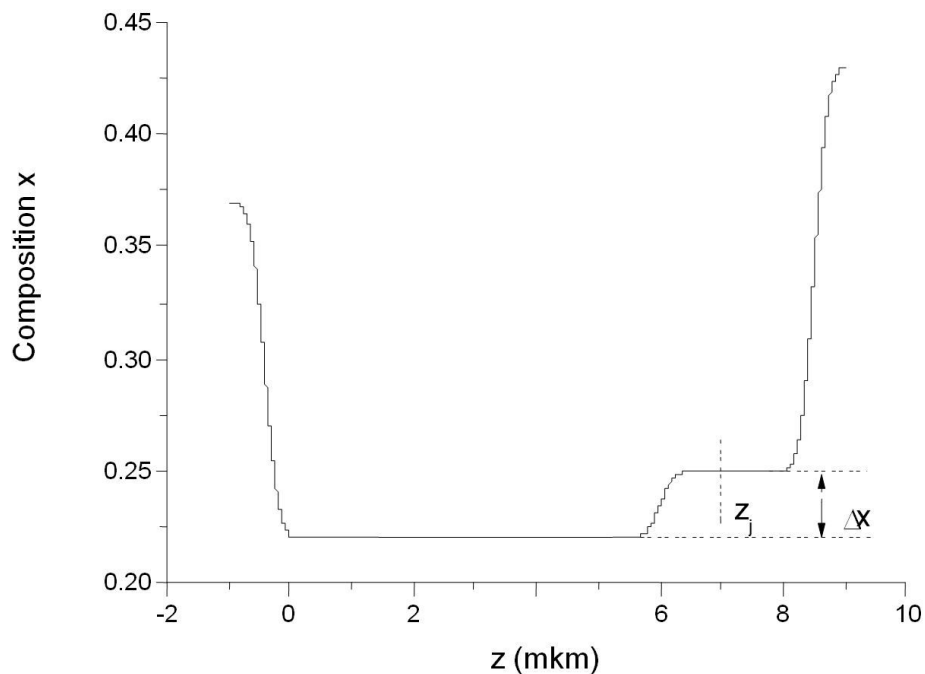


Figure 24. The MCT distribution throughout the thickness in p-P MCT HES: Δx – barrier between narrowgap and widegap parts of absorber layer; z_j – position of n - p junction.

The quantum efficiency η and $R_0 A$ product (R_0 – differential resistance at 0 bias voltage; A – diode area) was numerical calculated for p-P MCT HES taking into account only diffusion current in which the lateral diffusion current contribution becomes essential [21,22].

Fig. 25 shows the scheme of PV diode for calculation η and $R_0 A$. The MCT of narrow gap p and wide gap P layers is equal to 0.22 mole fraction CdTe and $0.22 + \Delta x$ mole fraction CdTe respectively. n - p junction located in P layer.

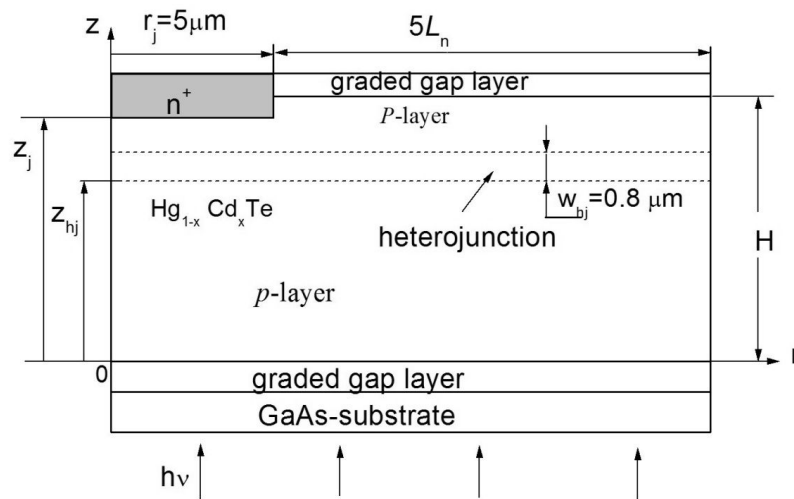


Figure 25. The scheme of n+-P-p diode fabricated in p-P MCT HES.

The diffusion current is determined from decision of stationary continuity equation for excess electron in p range. The valence band location in p-P absorber layer is permanent (common anion rule). The p -range is quasi neutral. The current in $n+$ range does not take into account. The stationary continuity equation in cylindrical coordinates at constant electron mobility and lifetime is expressed by

$$\frac{\partial^2 n'}{\partial r^2} + \frac{1}{r} \frac{\partial n'}{\partial r} + \frac{\partial^2 n'}{\partial z^2} - \frac{d}{dz} (\ln[n_i^2(z)]) \cdot \frac{\partial n'}{\partial z} - \left(\frac{d^2}{dz^2} \ln[n_i^2(z)] + \frac{1}{L_n^2} \right) \cdot n' = -\frac{g(z)}{D_n} \quad (13)$$

where $g(z) = \alpha(z) Q \exp(-\int_0^z \alpha(t) dt)$ $g(z)$ - generation function and $\alpha(z)$ – adsorption coefficient;

Q – the density of flux of radiation, n' - excess electron concentration, D_n - electron diffusion coefficient; L_n - electron diffusion length, n_i - intrinsic carrier concentration. The boundaries conditions are the following:

1. $\frac{\partial n'}{\partial r} = 0$ at $r = 0$ and $r = r_j + 5L_n$
2. $n' = n_{p0}(\exp(qV/kT) - 1)$ on n+-p junction borders
3. $\frac{\partial n'}{\partial z} = 0$ on the planar borders of absorber layer at $z = 0$ и $z = H$.

The incident radiation from back side of diode has wavelength for maximal ampere-watt sensitivity at 78 K.

The diode current I is determined after equation decision by integration of $j_N = qD_n \frac{\partial n'}{\partial z}$ and $j_L = qD_n \frac{\partial n'}{\partial r}$ on planar and lateral surfaces of n+-p junction. The $R_0 A$ product is determined from dark diffusion current I as $R_0 A = \frac{kT}{qI} A$, where $A = \pi r_j^2$ - area of n+-p junction. The quantum efficiency $\eta = \frac{I_p}{qQA}$ is determined by calculated photocurrent I_p .

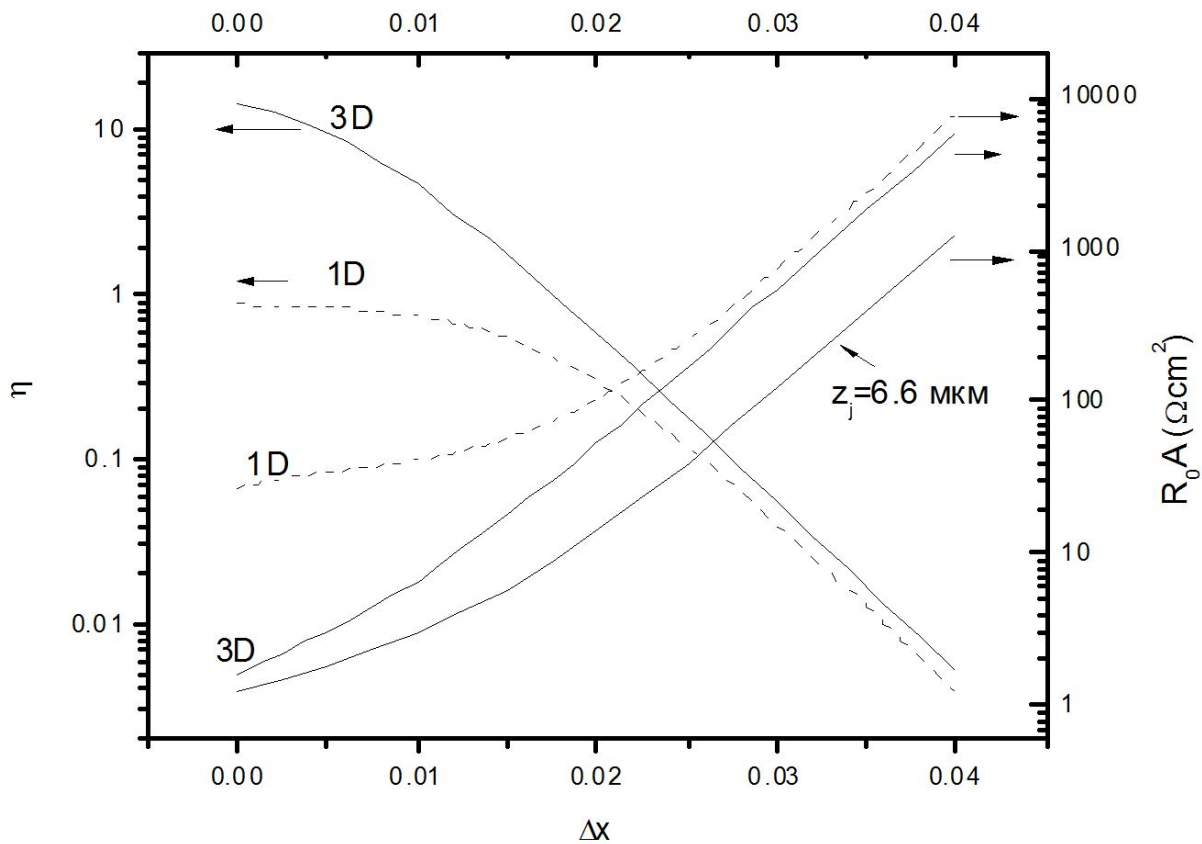


Figure 26. The $R_0 A$ and η для 1D and 3D diodes on Δx at $z_j = 8 \mu\text{m}$, $L_n = 25 \mu\text{m}$ and $r_j = 5 \mu\text{m}$.

Fig. 26 represents the dependence of $R_0 A$ and η on Δx . The Δx increasing leads to decreasing of diffusion current and changes the relationship between volume and lateral components from comparing $R_0 A$ and η for 3D and 1D diodes.

Fig. 27 (a, b) shows the influence of n+-p position and relationship r_j/L_n on diffusion current.

So the anyone using suggested model could be carried out the calculation and/or taking the data in Fig. 25, 26 to determine the MCT HES p-P construction (Δx , r_j and poison n+-p junction) which allows to fabricate IR detector with definite low diffusion current.

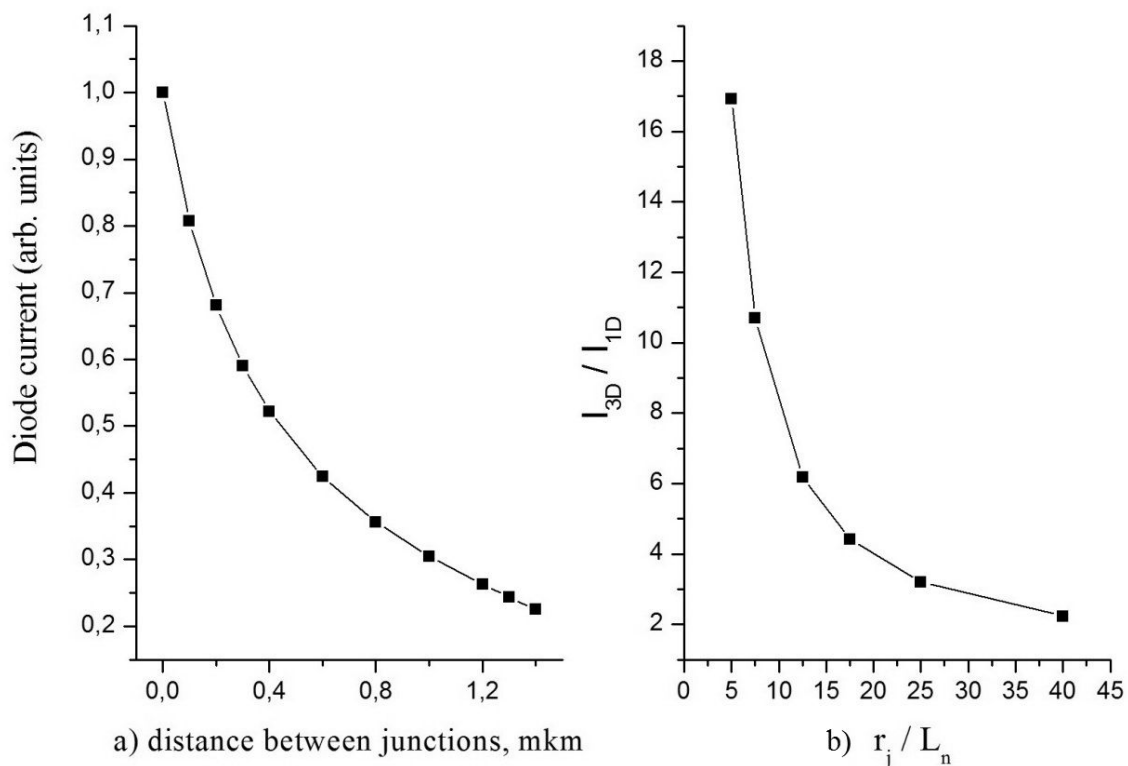


Figure 27. The diffusion current dependences on position of n+-p junction in P region (a) and relationship r_j / L_n (b).

4. The technology and parameters of IR detectors

4.1. Linear LWIR 288x4 FPA

The linear 288x4 PV FPA has been fabricated by planar technology described in [23] using MCT HES with graded widegap layer at absorber layers boundaries represented in Fig. 13. The FPA has 288 channels of four pixels, on which time delay and integration (TDI) is performed through the readout integrated circuit (ROIC). The size of each pixel is 25 μm (scan direction) per 28 μm (cross-scan direction). The in-scan pitch is 43 μm and the cross-scan pitch is 28 μm . The diodes were formed by the implantation of B⁺ ions with the energy ~50 keV and a dose $\sim 3 \times 10^{13} \text{ cm}^{-2}$ into p-MCT structures. The spectral response of one of the element in the array is shown in Fig. 28, (STD = 0.1 μm).

Current-voltage characteristics of 30 diodes have been measured at random with the help of the microprobe device cooled by the liquid nitrogen vapour. The typical dark current was equal to 5.3 nA at the reverse bias voltage 150 mV.

A defect diode can be detected by its high dark current, and the deselection function of the ROIC allows us to switch such a diode off. The time delay integration is performed over the entire 4-diode channel thus, the presence of a single defect diode does not influence the

channel operation. Additionally, there is an option in the ROIC to use the average dark current value for deselected defect diodes.

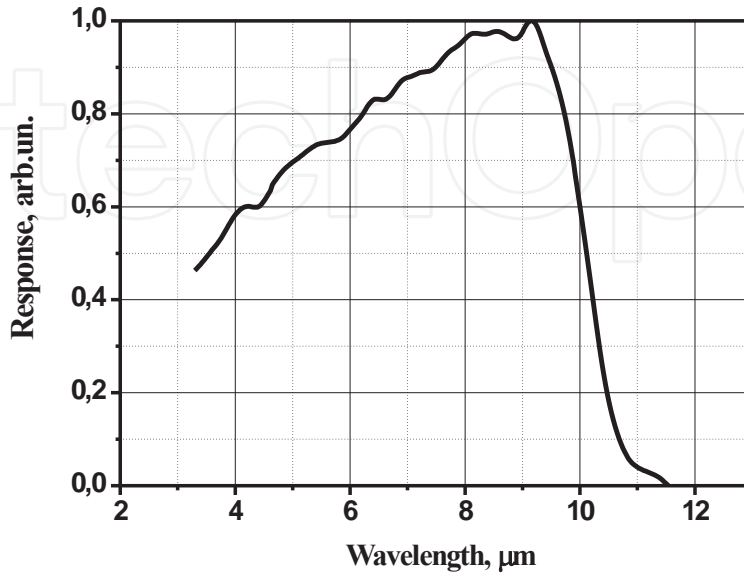


Figure 28. The typical spectral response of one of the sensitive element in 288x4 PV FPA.

In Fig. 29, the typical I-V curve and differential resistance R versus bias voltage at 77 K are shown. The values of R_0 , R_{max} and of the product $R_0 A$ were equal to $1.6 \times 10^7 \Omega$, $2.1 \times 10^8 \Omega$, and $70 \Omega \text{ cm}^2$, respectively.

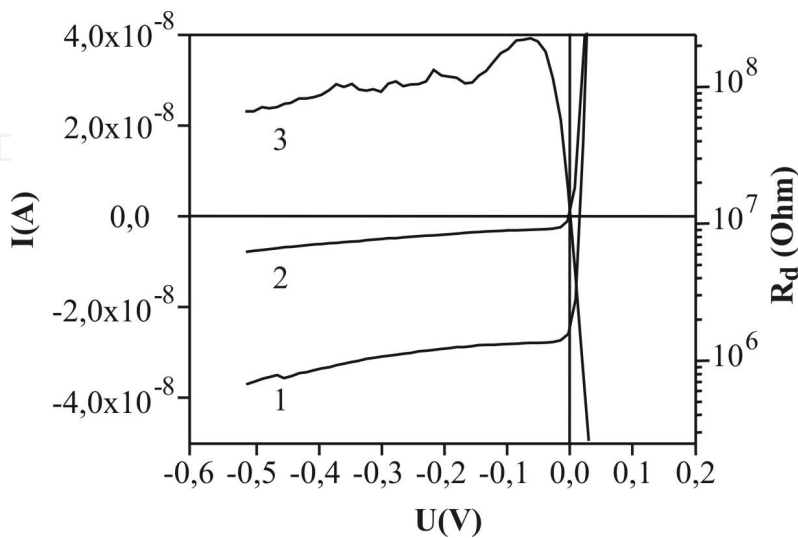


Figure 29. The typical current (1 – the photocurrent, 2 - the dark current) and the differential resistance (3) dependence on the bias voltage.

The experimentally measured I-V curves of photodiodes has been modelled with the help of the carrier balance equations approach [24,25], assuming the presence of in-gap donor-type trap level with the energy $E_t \approx 0.7E_g$ and taking into account the trap-assisted tunnelling and the Shockley-Read-Hall (SRH) generation/recombination as two current mechanisms. The other relevant current mechanisms, that do not involve the trap levels, have been taken into account additively. The modelling has shown that at a small reverse bias (less than -0.25 V) the dark current is limited by the diffusion current and the SRH current outside the n - p -junction. At the reverse bias larger than -0.25 V, the dark currents were determined by the tunnelling and thermal generation from the trap levels. Interband tunnelling as well as the other recombination mechanisms do not contribute substantially at the operational bias values. The modelling has shown that these heterostructures are of the $n^+ - n^- - p$ type, with the n - p junction shifted into n -region that is characterized by long carrier lifetimes and low concentration of recombination centres (due to the compensation of the Hg vacancies). The use of the varyband potential at the surface of the heteroepitaxial MCT structure allows us to increase the effective carrier lifetime by means of diminishing the influence of the surface recombination, as well as by suppressing the surface leakage currents [26].

Experimentally, our average diodes have shown current-voltage characteristics that are practically limited by the diffusion current mechanism for ideal diodes. Such characteristics make possible to realize the FPA operating in a BLIP regime.

The multiplexer was designed using the $1.0\text{-}\mu\text{m}$ CMOS technology with two polysilicon and two metallic layers. The multiplexer provides a bidirectional TDI scanning, random pixel deselection, anti-blooming and background skimming, and testing analogue part of a circuit without connection to photodiodes. The output charge capacity of the multiplexer exceeds 2.5 pC at the nonlinearity lower than 2%.

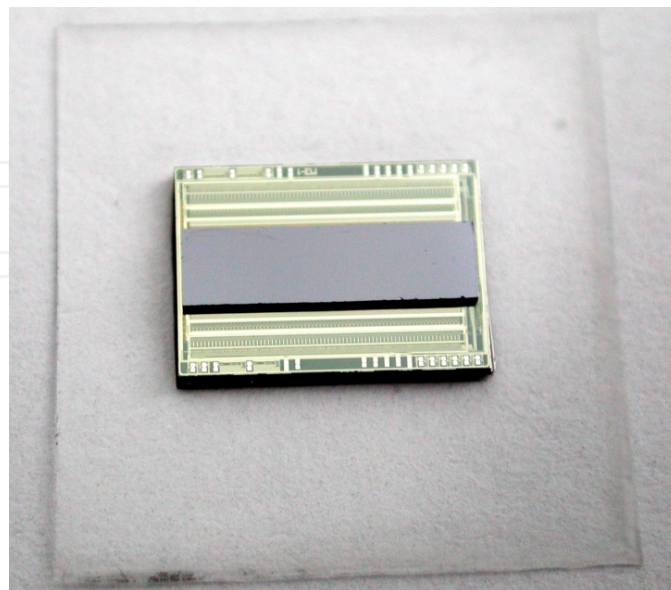


Figure 30. The photo view 288x4 PV FPA hybrid assembly.

The 288×4 PV FPA was fabricated by hybrid assembling of the photosensitive array and the ROIC, with the help of indium bumps group welding at 120°C. After hybridization, the total height of In bumps was equal to ~10 μm [27]. In Fig. 30, a photo of the 288×4 PV FPA hybrid assembly is presented.



Figure 31. An example of the thermal image 288×4 PV FPA.

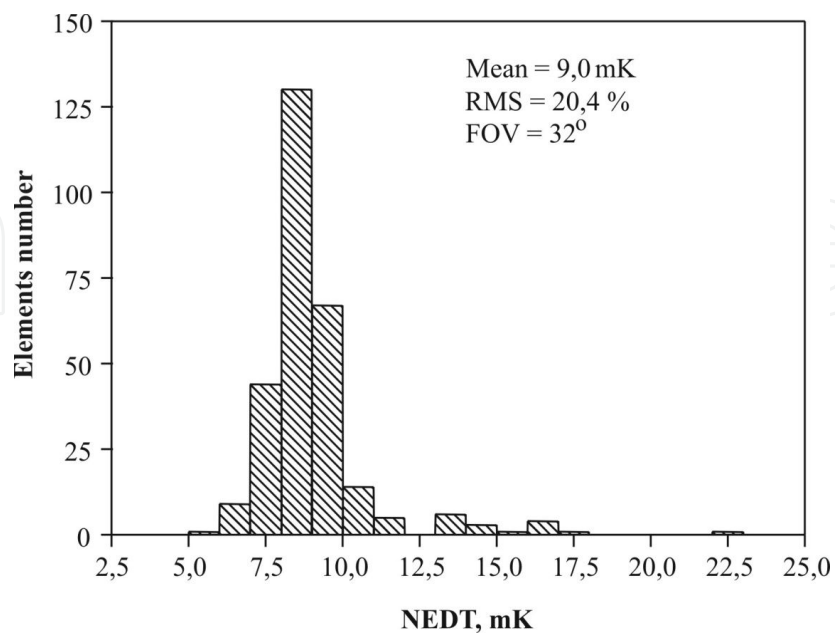


Figure 32. The histogram of NETD.

The measurement of PV FPA parameters were carried out in a cryostat at 77 K, the input signal was coming through the GaAs substrate (FOV 32°, 295 K). The integration time was 20 μ s. Typical values of responsivity and detectivity at the maximum of the spectral sensitivity were equal to 2.27×10^8 V/W and 2.13×10^{11} $\text{cm} \times \text{Hz}^{1/2} \times \text{W}^{-1}$ at STD 6.7% and 15.3%, respectively. The example of a 576 \times 610 thermal image by PV FPA (FOV = 32°, F = 1/1.6) is presented in Fig. 31.

The NETD histogram is shown in Fig. 32. The average NETD value is about 9 mK.

4.2. Matrix LWIR 320 \times 256 PV FPA

We developed the technology of fabricating 320 \times 256 (320 \times 240) and 320 \times 240 PV FPA operated in wavelength ranges 8-12 μ m at 77 K. The MCT HES composition distribution throughout the thickness used for FPA is analogous presented in Fig. 14.

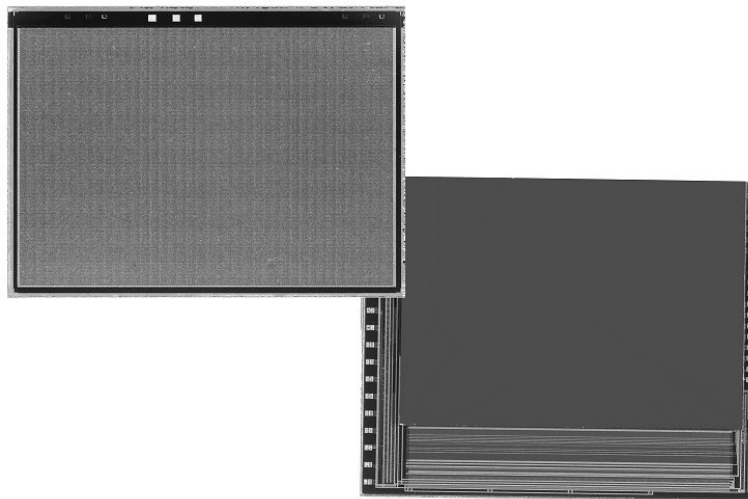


Figure 33. The photo view 320 \times 240 PV.

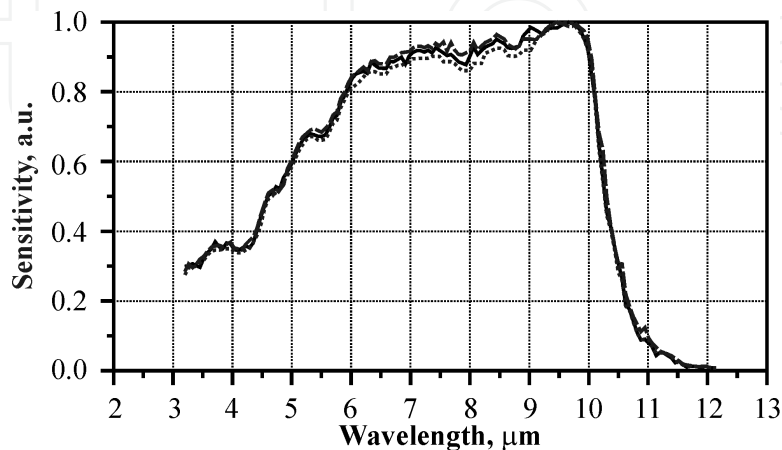


Figure 34. Spectral responsivity 320 \times 240 PV FPA.

The topology 320×256 (320×240) FPA is matrix with pixel pitch 30 μm in X и Y directions. Fig. 33 shows photo view of 320×240 FPA (photosensitive pixels array in left corner).

The typical spectral response is present in Fig. 34.

The low dark current is equal to 1.5-2 nA and is constant up to reverse bias voltage 200 mV for best diodes. The product $R_0 A=40 \text{ Ohm}\times\text{cm}^2$ for such diode (optical area $A=8\times 10^{-6} \text{ cm}^2$) is compatible to the best literature data for $n^+ - p$ photodiodes [17]. The readout integrated circuit 320×256 design is based on a silicon CMOS technology. The charge capacity is very large - more then 20 pC. This multiplexer can operate with LWIR photodiodes for spectral range to 14 μm , that have large dark and background current. Developed multiplexer operate with two formats: 320×256 and 320×240 elements. IR FPA was fabricated by hybrid cold welding by indium bumps of photodiode array and silicon ROIC under pressure. The F/1,6 NEDT and thermal images with the help of LWIR 320×240 FPA are shown in Fig 35, 36.

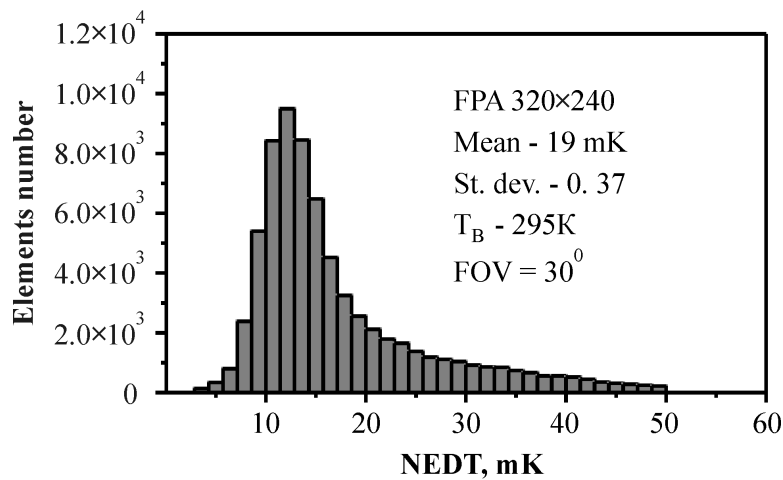


Figure 35. NEDT histogram of 320×240 PV FPA.



Figure 36. Thermal images 320×240 PV FPA.

4.3. Heterodyne LWIR detector

The HF PD threshold heterodyne detection power (P_t) taking into account real parameters described by the expression (1)

$$P_t = \left[\frac{P_d^2}{2P_g} + \frac{\hbar\omega_s}{\eta(\omega_s - \omega_g)} \right] \quad (14)$$

where P_d – threshold power at baseband detection;
 P_g – heterodyne power, ω_s – frequency of detected radiation,
 ω_g – heterodyne frequency, $\eta(\omega_s - \omega_g)$ – quantum efficiency.

In Fig. 37 the calculation solid curves (1-3) of P_t dependences on P_g for different P_d are shown.

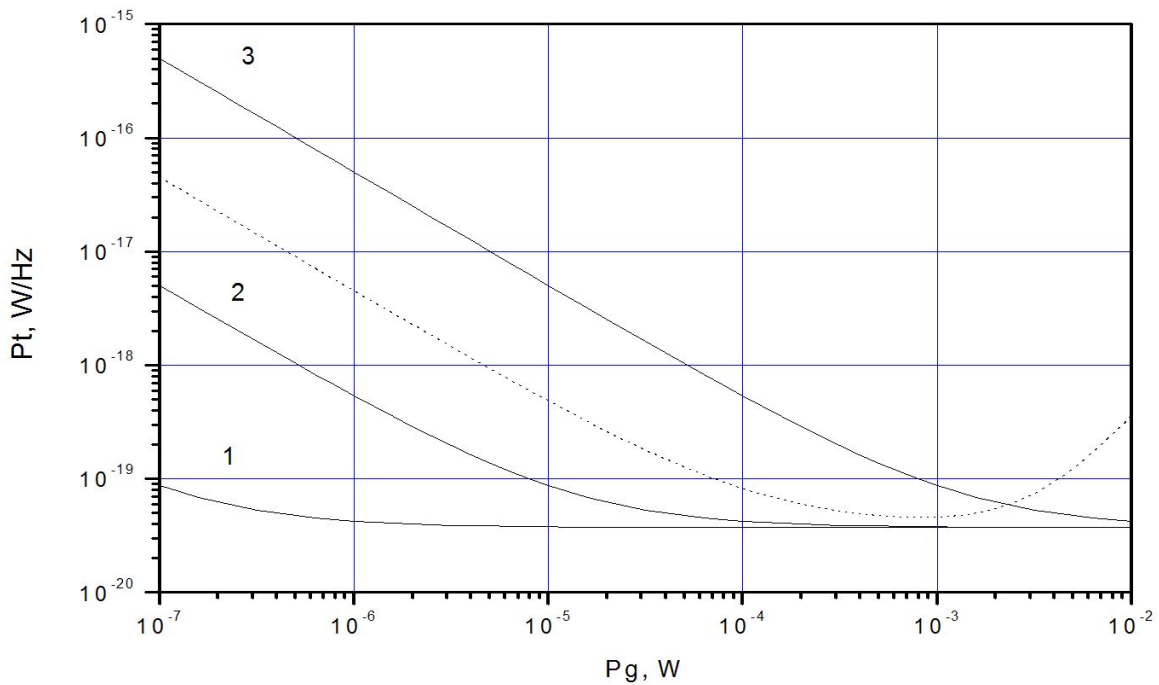


Figure 37. The dependences of P_t on P_g of HF PD for detection 10,6 μm wavelength radiation at $\eta = 0,5$: 1 - $P_d = 10^{-13}$ $\text{W}/\text{Hz}^{1/2}$; 2 - $P_d = 10^{-12}$ $\text{W}/\text{Hz}^{1/2}$; 3 - $P_d = 10^{-11}$ $\text{W}/\text{Hz}^{1/2}$.

The dashed line is typical experimental data. It is clear that theoretically P_t values reach minimum value at essentially smaller P_g for PD's with the minimal P_d values. Experimental P_t values for PD's based on bulk p-type HgCdTe (dashed line) has analogous dependence on P_g . But at $P_g > 10^{-3}$ W P_t begin increases that connected with changing optimal condition operation because of PD heating. So it is necessary to fabricate PD with smaller P_d values for favorable operation condition. And it is maybe important for multi-channel system having low heterodyne radiation power. We fabricated HF PD on the basis of p-type MCT HES (see

Fig. 15) with thickness of absorber ~ layer 10 μm. The calculations and experimental data were shown that it is necessary to grow wide gap layer between high conductivity narrow gap layer and absorber to reach limiting PD and HF PD parameters [23]. The QE of PD on the basis HgCdTe HS MBE without antireflection coating $\eta \cong 0.65$. The $R_s < 10 \Omega$ and $R_o \times A = 100 \div 130 \Omega \text{ cm}^2$. The $S_v (\lambda=15.0 \mu\text{m})$ and $D^* (\lambda=15.0 \mu\text{m})$ were $(5 \div 7) \times 10^5 \text{ V W}^{-1}$ and $(6 \div 8) \times 10^{10} \text{ cm Hz}^{1/2} \text{ W}^{-1}$ at $\text{FOV}=30^\circ$ and $T_{\text{background}} 295\text{K}$.

The specification of single element HF PD and PC is the following:

	PD	PC
Element size, μm	250	100×100
λ_{max} , μm	10	15
$\lambda_{0,1}$, μm	11	19
Pd (λ_{max}), W/Hz ^{1/2}	2×10^{-13}	1×10^{-13}
Pt (λ_{max}), W/Hz	10^{-19}	10^{-18}
operating temperature, K		77-78K
frequency range, GHz		≥ 1

Table 2

HF PD and PC mounted into LN₂ cooled Dewar (Fig. 38).

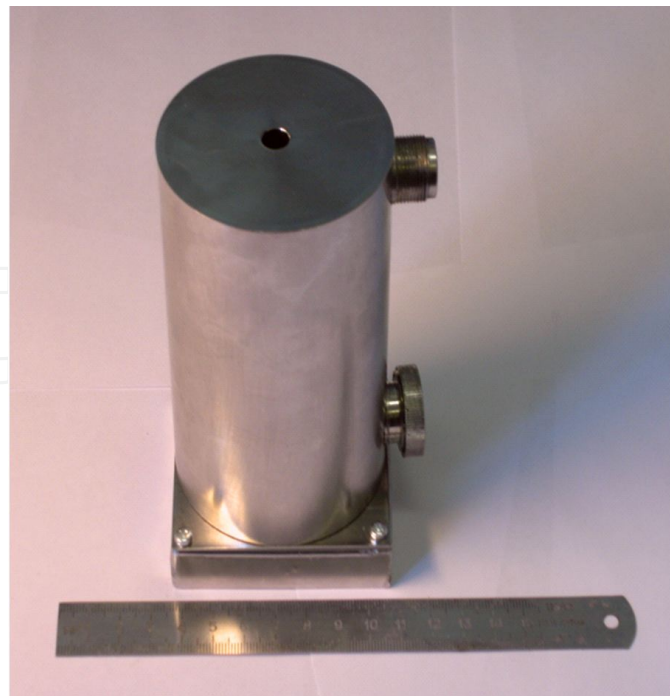


Figure 38. The view HF PD into LN₂ Dewar.

4.4. Matrix LWIR 128×128 PV FPA

We fabricated 128×128 PV FPA by planar low temperature technology on the basis of p-P MCT HES (see Fig. 24). N⁺ - P junctions were fabricated by B⁺ implantation and located into MCT P-layer. The photodiode parameters were as following: λ_c = 10,6 μm; dark current 0,8 nA at V = -200 mV at 77K. The diodes pitch was 40 μm. The diode size was 17×17 μm. The wavelength cut off was 10,3μm. The diode design and band diagram was shown in Fig. 39.

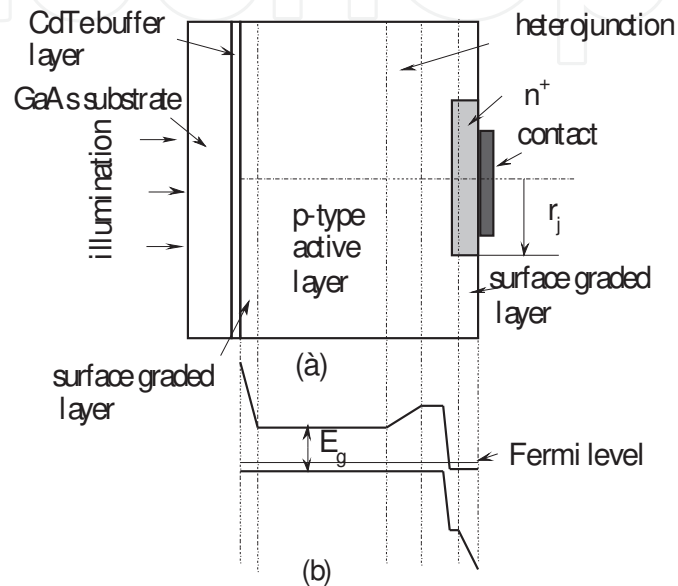


Figure 39. Photodiode base on p-P MCT HES : (a) design and (b) band diagram.

The ratio signal to noise (S/N) of hybrid FPA expressed by well-known equation

$$S/N = I_s/I_y \times (k \times Q/q)^{1/2} \quad (15)$$

where I_s – the signal photocurrent, I_y – total current, equal to sum of dark current and background current (neglecting the signal current), k – the charging of accumulating capacitance coefficient, Q – charge capacitance, q – electron charge.

The relation S/N of FPA based on P-p NCT HES does not depend on barrier height because of decreases at presence of potential barrier at the same manner of photo- and dark currents at diffusion approximation. Nevertheless, in real diode frequently there is existed an excess 1/f noise and dark current caused by generation and tunneling processes inside space-charge region. In this situation large photocurrent through high-resistance p-absorber to ground bus leads to large differences of voltage biases of FPA photodiodes at the center and periphery. It appears as an additional noise increase. Moreover ROIC added noise according to $I_n = V_n/R_d$, where I_n – noise current, V_n – bias noise voltage, R_d – differential resistance

which may be essential values at small R_d . So, in real FPA values S/N is usually lower than calculated one by formula (1). This difference is increase with the increase total diode current. The potential barrier at P-p MCT HES leads to decrease of total diode current of FPA and eliminates negative phenomena described previously. We showed from measurement of noise spectrum that frequency cut off of $1/f$ noise for photodiode on the basis of P-p MCT HES is equal up to less than 10 Hz. These $1/f$ values are essentially lower than for FPA based on MCT epitaxial structure without P-p heterojunction. It means that S/N of FPA on the basis P-p heterojunction will approach to values given by equation 16.

128×128 hybrid FPA was package inside cooled cryostat with ZnSe window. We measured the FPA parameters in range 77 – 300K, at FOV 45°, black body temperatures 300 - 500K and background temperature 295K. The temperature at measurement maintained with accuracy 0,5K. We measured the black body's diode signal and noise. The signal storage time satisfied by $k = 0,8$. The S/N experimental (squares) data of FPA on the basis of P-p MCT HES are given in Fig. 40.

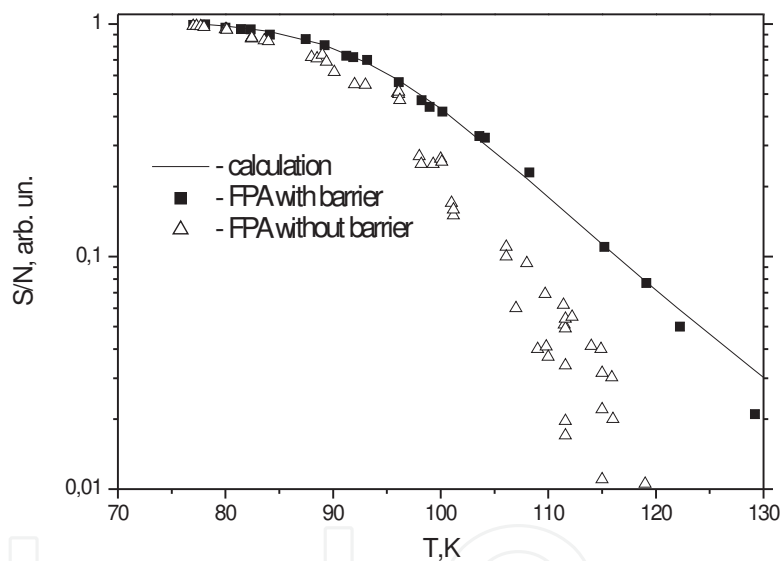


Figure 40. The ratio of S/N on temperature. Squares – FPA on p-p MCT HES. Triangles – FPA on p-type MCT HES. Solid curve – calculation.

In the same Figure the calculated S/N dependence is shown for analogous FPA without barrier at the same measurements regime. The S/N calculation was carried out in following approximations:

- the dark current was calculated by diffusion model;
- the velocity of surface recombination on boundaries was zero;
- the carrier collection area at fixed temperature was determined by geometric size of n-region and carrier diffusion length but was no more than pixel size;

- quantum efficiency value was taken to be 0.7;
- 1/f noise was zero;
- the accumulation time was chosen from the above condition of charging of accumulation capacitance.

In the same Figure measured S/N values are given for few FPA on the basis of MCT layer without P-p barrier with λ_c in range 10,5-10,7 μm at $T=77\text{ K}$.

The experimental S/N values of FPA on the basis of P-p DLHJ with barrier more closely correspond to calculated dependence in comparison with FPA on the basis of MCT layer without P-p barrier. This can be explained as follows. At temperatures near 77 K lower S/N ratio of FPA on the basis of MCT layer without P-p barrier is associated to excess currents (generation and tunneling current) and to presence of 1/f noise. When the temperature increases in range 77 -130K the diodes differential resistance of FPA diodes decreases and total current increases. The first leads to increase of ROIC noise and diodes noise. The second leads to additional noise determined by strong mutual coupling of photodiodes. All this factors decrease the S/N ratio faster than calculated one. It means that FPA for operating at elevated temperatures must be fabricated on the basis of P-p DLHJ with barrier. The behavior of S/N will analogous ones which given in Fig.4 for at increase of wavelength cut off at constant operating temperature.

5. Conclusion

The technology of fabrication of mercury cadmium telluride (MCT) heterostructure (HES) at growth by molecular beam epitaxy (MBE) was developed. The MBE ultra vacuum set allows to grow high quality n-type MCT HES with monitoring in real time. Thermal treatments are used for fabrication high quality p-type MCT HES for LWIR photovoltaic (PV) devices.

We suggested different MCT HES design with graded widegap layers, high conductivity layer and p-P structures.

We demonstrated the four cooled LWIR detectors for spectral range 8-11 μm based on these MCT HES:

- linear 288×4 PV FPA on the basis MCT HES with graded widegap layers on the boundaries of absorber layer;
- matrix 320×256(240) PV FPA on the basis MCT HES with high conductivity layer (growing by doping) to eliminate “debiasing” effect;
- matrix 128×128 PV FPA on the basis MCT HES with p-P absorber layer which successfully operated at elevated temperature;
- one elements heterodyne detector on the basis MCT HES with high conductivity layer (growing narrowgap layer) operating at GHz frequencies.

The parameters of these devices are limited by background radiation.

Author details

V. V. Vasiliev¹, V. S. Varavin¹, S. A. Dvoretzky^{1*}, I. M. Marchishin¹, N. N. Mikhailov¹, A. V. Predein¹, I. V. Sabinina¹, Yu. G. Sidorov¹, A. O. Suslyakov¹ and A. L. Aseev¹

*Address all correspondence to: dvor@isp.nsc.ru

1 A.V. Ryhanov Institute of Semiconductor Physics, Siberian branch of the Russian academy of sciences, Russia

References

- [1] Massies, J., & Contour, J. P. (1985). Substrate chemical etching prior to molecular-beam epitaxy: An x-ray photoelectron spectroscopy study of GaAs {001} surfaces etched by the H₂SO₄-H₂O₂-H₂O solution. *Journal of Applied Physics*, 58(2), 806-810.
- [2] Bondar', D. N., Varavin, V. S., Obidin, Yu. V., Petukhov, K. V., & Mikhailov, N. N. (2005). An automated system for inspection of growth defects on heteroepitaxial structures. Proceedings of ACIT-2005, Automation, Control, and Information Technology June 20-24 Novosibirsk, Russia (in Russian), 207-211.
- [3] Chang, C., Helblum, M., Ludeke, R., & Natan, M. I. (1981). Effect of substrate surface treatment in molecular beam epitaxy on the vertical electronic transport through the film-substrate interface. *Applied Physics Letters*, 39, 229-231.
- [4] Cho, A. I. (1983). Growth of III-V semiconductors by molecular beam epitaxy and their properties. *Thin Solid Film*, 100, 291-296.
- [5] Vasques, R. P., Lewis, B. F., & Grunthner, F. J. (1983). X-ray photoelectron spectroscopic study of the oxide removal mechanism of GaAs(100) molecular beam epitaxial substrates in in situ heating. *Applied Physics Letters*, 42(3), 293-295.
- [6] Vasques, R. P., Lewis, B. F., & Grunthner, F. J. (1983). Cleaning chemistry of GaAs(100) and InSb(100) substrates for molecular beam epitaxy. *J. Vacuum. Science and Technology*, B1, 791-794.
- [7] Zubkov, V. A., Kalinin, V. V., Kuz'min, V. D., Yu, G., Sidorov, S. A., & Dvoretzky, S. I. (1991). Stenin. The investigation of initial growth stages of CdTe on (001)GaAs at molecular beam epitaxy. *Poverkhnost (Phyzika, Chemistry, Mechanics)* (in Russian) (9), 45-51.
- [8] Otsuka, N., Kolodziejski, L. A., Gunshor, R. L., & Datta, S. (1985). High resolution electron microscope study of epitaxial CdTe-GaAs interfaces. *Applied Physics Letters*, 46(9), 860-862.
- [9] Tatsuoka, H., Kuwabara, H., Fujiyasu, H., & Nakanishi, Y. (1993). Growth of CdTe on GaAs and its stress relaxation. *Journal of Applied Physics*, 65, 2073-2077.

- [10] Pesek, A., Ryan, T. W., Sasshofer, R., Fantner, E. J., & Lischka, K. (1990). Investigation of the CdTe/GaAs interface by the x-ray rocking curve method. *Journal of Crystal Growth*, 101, 589-593.
- [11] Varavin, V. S., Dvoretzky, S. A., Liberman, V. I., Mikhailov, N. N., & Sidorov, Yu. G. (1995). The controlled growth of high-quality mercury cadmium telluride. *Thin Solid Films*, 267, 121-125.
- [12] Varavin, V. S., Dvoretzky, S. A., Liberman, V. I., Mikhailov, N. N., & Sidorov, Yu. G. (1996). Molecular beam epitaxy of high quality $\text{Hg}_{1-x}\text{Cd}_x\text{Te}$ films with control of the composition distribution. *J. Cryst. Growth*, 159, 1161-1166.
- [13] Konstantinov, O. V., & Tsarenkov, G. V. (1976). Photoconductivity and Dember effect in graded semiconductors. *Fizika i Tekhnika Poluprovodnikov (in Russian)*, 10(4), 720-725.
- [14] Rogalski, A., & Piotrowski, J. (1988). Intrinsic infrared detectors. *Progress in Quantum Electronic*, 12(1), 87-118.
- [15] Matore, H. F. (1971). *Defect Electronics in Semiconductors*, NY-London, Wiley.
- [16] Musca, C. A., Siliquini, J. F., Fynn, K. A., Nener, B. D., Faraone, L., & Irvine, S. J. C. (1996). MOCVD-grown wider-bandgap capping layers in HgCdTe long-wavelength infrared photoconductors. *Semiconductor Science and Technology*, 11(12), 1912-1917.
- [17] Rogalski, A. (2000). *Infrared Detectors*, Gordon and Breach Science Publisher.
- [18] Varavin, V. S., Vasiliev, V. V., Dvoretzky, S. A., Mikhailov, N. N., Ovsyuk, V. N., Sidorov, Yu. G., Suslyakov, A. O., Yakushev, M. V., & Aseev, A. L. (2003). HgCdTe epilayers on GaAs: growth and devices. *Optoelectronics Review*, 11(2), 99-111.
- [19] Varavin, V. S., Vasiliev, V. V., Zakhariash, T. I., et al. (1999). Photodiodes with low series resistance with graded band gap HgCdTe epitaxial films. *Journal of Optical Technology*, 66, 69-72, (in Russian).
- [20] Vasiliev, V. V., Dvoretzky, S. A., Varavin, V. S., Mikhailov, N. N., Remesnik, V. G., Sidorov, Yu. G., Suslyakov, A. O., Yakushev, M. V., & Aseev, A. L. (2007). Matrix detector on the basis of p-P MCT HES grown by MBE. *Avtometriya*, 43(4), 17-24, (in Russian).
- [21] Wenus, J., Rutkowski, J., & Rogalski, A. (2001). Two-dimensional analysis of double-layer heterojunction HgCdTe photodiodes. *IEEE Trans. Electron. Devices*, 48(7), 1326-1332.
- [22] Dhar, V., & Gopal, V. (2001). Dependence of zero-bias resistance-area product and quantum efficiency on perimeter-to-area ratio in a variable-area diode array. *Semiconductor Science and Technology*, 16(7), 553-561.
- [23] Vasiliev, V. V., Dvoretzky, S. A., Varavin, V. S., Mikhailov, N. N., Sidorov, Y. G., Zakharyash, T. I., Ovsyuk, V. N., Chekanova, G. V., Nikitin, M. S., Lartsev, I. Y., &

- Aseev, A. L. (2001). MWIR and LWIR detectors based on HgCdTe/CdZnTe/GaAs heterostructures. *Proceedings SPIE*, 5964, 75-87.
- [24] Gumenjuk-Sichevska, J. V., & Sizov, F. F. (1999). Currents in narrow-gap photodiodes. *Semiconductor Science and Technology*, 14, 1124-1133.
- [25] Sizov, F. F., Lysiuk, I. O., Gumenjuk-Sichevska, J. V., Bunchuk, S. G., & Zabudsky, V. V. (2006). Gamma radiation exposure of MCT diode arrays. *Semiconductor Science and Technology*, 21, 358-363.
- [26] Andreeva, E. V., Varavin, V. S., Vasiliev, V. V., Gumenjuk-Sichevska, J. V., Dvoret-sky, S. A., Mihajlov, N. N., Tsybtii, Z. F., & Sizov, F. F. (2009). Comparison of current characteristics of CdHdTe photodiodes grown by MBE and LPE methods. *Journal of optical Technology*, 76, 42-48.
- [27] Vasiliev, V. V., Varavin, V. S., Dvoret-sky, S. A., Mikhailov, N. N., Ovsyuk, V. N., Si-dorov, Yu. G., Suslyakov, A. O., Yakushev, M. V., & Aseev, A. L. (2003). HgCdTe epi-layers on GaAs: growth and devices. *Opto-Electronics Review*, 11, 99-111.